UNIVERSITÀ
DEGLI STUDI
DI PADOVA

DIPARTIMENTO
DI INGEGNERIA
DELL'INFORMAZIONE

INFORMATION ENGINEERING DEPARTMENT

DEGREE COURSE IN INFORMATION ENGINEERING

THE PLUS ULTRAVIOLET SPECTOGRAPH FOR THE OBSERVATION OF PLANETARY EXOSPHERES

SUPERVISOR
Prof.ssa Maria-Guglielmina Pelizzo

CO-SUPERVISOR
Marta Padovani

GRADUAND
Sara Petrelli

ACADEMIC YEAR
2021-2022

GRADUATION DAY
19th September 2022

Abstract

Ultraviolet spectographs are of key importance in Solar physics, in the physics of interstellar medium and in the planetary exospheres studies. The best technique to probe the exospheres and the highest-altitude atmospheres of planets and satellites is in fact the FUV/EUV (Far/Extreme Ultraviolet) imaging spectrometry; it allows to determine constituents and dynamics of the atmosphere, to understand its formation mechanisms and surface release processes.

This work focuses its attention on the presentation of the most recent Ultraviolet spectograph: PLUS (PLanetary Ultraviolet Spectrometer), and provides the description of two experimental activities related to the project, in which I was actively involved at CNR-IFN laboratory.

PLUS is a two channels high performance spectrograph which will be used to observe planetary exospheres in the 55-200 nm range, where there are significant spectral features. It is a state of the art scientific device in the study of planetary exospheres, since it improves the performance thanks to high efficiency optical components optimized for each channel and a simplified design.

The first activity performed at the laboratory is related to the vacuum chamber and the gratings' mounts inside it, my role has been to start up the controller and understand how to move the gratings' supports in order to realise the desired alignment. The second activity aimed to obtain the calibration of the slit width with respect to the position of a knob able to change this width. For this purpose, I have extracted the sought value from the diffraction figure, obtained by illuminating the slit with a laser beam, for three different positions of the knob.

The project funding started in 2020 and should last until December 2022, it has been granted within the implementation agreement ASI (Agenzia Spaziale Italiana)-INAF (Istituto Nazionale di AstroFisica) n.2018-16-HH.0 in relation to ”Attività di Studio per la comunità scientifica nazionale SOLE, SISTEMA SOLARE ED ESOPIANETI”, which wants to support the study of Sun, Solar Systems and Exoplanets. Currently, researches from CNR-IFN Padova, INAF/IASF Milano, Politecnico di Milano and University of Padua are working on the PLUS project.

Sommario

Gli spettrografi Utravioletti sono di fondamentale importanza nella fisica del Sistema Solare, del mezzo interstellare e negli studi delle esosfere planetarie. La migliore tecnica per sondare le esosfere e le atmosfere ad alta quota di pianeti e satelliti è infatti la spettrometria per immagini nell'intervallo FUV/EUV (Far/Extreme Ultraviolet); questa permette di determinare elementi e dinamiche dell'atmosfera, di comprenderne i meccanismi di formazione ed i processi di rilascio superficiale.

Questo scritto concentra la sua attenzione sulla presentazione del più recente spettrografo ultravioletto: PLUS (PLanetary Ultraviolet Spectrometer), e fornisce la descrizione di due attività sperimentali legate al progetto a cui ho partecipato attivamente al laboratorio del CNR-IFN.

PLUS è uno spettrografo a due canali con performance migliorate che sarà utilizzato per osservare le esosfere planetarie nell'intervallo 55-200 nm, dove vi sono caratteristiche spettrali significative. É uno strumento scientifico all'avanguardia nello studio delle esosfere planetarie, infatti migliora le performance rispetto a quelli precedenti, grazie alle componenti ottiche ad alta efficienza ottimizzate per ogni canale e ad un design semplificato.

La prima attività svolta in laboratorio riguarda la camera a vuoto ed i supporti dei reticoli che si trovano al suo interno, il mio ruolo è stato quello di attivare il controllore e comprendere come muovere questi supporti al fine di realizzare l'allineamento desiderato. La seconda attività ha avuto l'obiettivo di ottenere la calibrazione della larghezza della fenditura in funzione della posizione di una manopola in grado di modificare questa larghezza. A tale scopo, ho estratto il valore cercato dalla figura di diffrazione, ottenuta illuminando la fenditura con un fascio laser, per tre diverse posizioni della manopola.

Il finanziamento del progetto è iniziato nel 2020 e dovrebbe durare fino a Dicembre 2022, esso è stato erogato in virtù dell'accordo attuativo ASI (Agenzia Spaziale Italiana)-INAF (Istituto Nazionale di AstroFisica) n.2018-16-HH.0 relativo ad "Attività di Studio per la comunità scientifica nazionale SOLE, SISTEMA SOLARE ED ESOPIANETI", il quale vuole supportare lo studio del Sole, del Sistema Solare e degli Esopianeti. Attualmente, ricercatori del CNR-IFN Padova, dell' INAF/IASF Milano, del Politecnico di Milano e dell'Università di Padova stanno lavorando al progetto PLUS.

Contents

List of Figures **3**

1 PLUS scientific objectives **5**
- 1.1 Science framework 5
- 1.2 Background 9
- 1.3 Scope of PLUS 14

2 Instrument description **17**
- 2.1 Optical scheme 18
- 2.2 Grating Components 20
- 2.3 Detectors 21
- 2.4 The system and the EUV channel demonstrator 24

3 Experimental activities **29**
- 3.1 XILab software 29
  - 3.1.1 Settings 32
  - 3.1.2 Commands 35
- 3.2 Slit width calibration 36
  - 3.2.1 Theory of diffraction 36
  - 3.2.2 Image acquisition and relative fitting 39
  - 3.2.3 Results 41

Conclusions **45**

Bibliography **48**

List of Figures

1.1 Moon's image 5
1.2 Possible observation modes 6
1.3 Mercury's image collage from MESSANGER spacecraft 6
1.4 EUV detector image and spectrum for Argon gas: HV=-3436 V [5] (Levels are in log_{10}-scale) 8
1.5 Summary of the main spectrometer parameters [6] 10
1.6 PHEBUS inner view [11] 10
1.7 PHEBUS optical layout [4] 11
1.8 The MPO and MMO in Mercury orbit [13] 12
1.9 1^{st} Bepi-Colombo Mercury flyby in 2021 12
1.10 MESSENGER in Mercury orbit 12

2.1 PLUS optical layout [15] 18
2.2 PLUS optical configuration parameters [15] 19
2.3 EUV channel *SiC* plane grating prototype with *SiC* thickness of 70 nm and 1200 lines/mm [6] 20
2.4 FUV channel Al/MgF_2 plane grating prototype with Al/MgF_2+Cr thickness of 75 nm [6] 20
2.5 The PLUS detector 21
2.6 Pixel readout chain of MIRA ASIC [17] 22
2.7 PLUS Opto-mechanical concept 24
2.8 Opto-mechanical parts for the EUV channel demo realisation [6] 25
2.9 Picture of vacuum chamber for the EUV channel demo realisation 25
2.10 Picture of the inside of the vacuum chamber 25
2.11 MCP Chevron assembly [16] 26
2.12 MIRA first release with a zoom view of the pixel structure [16] 26
2.13 Detector prototype assembly [16] 27

3.1 Rotations' axes 29
3.2 Standa motorised stages used inside the vacuum chamber 29

3.3 8SMC5-USB - Stepper & DC Motor Controller 30
3.4 Explanation of the controller flashes 30
3.5 XILab main window possible modes 31
3.6 8SMC5-USB Controller Specifications [18] 32
3.7 XILab Settings Main Window 32
3.8 Slit picture 36
3.9 Single-slit diffraction 37
3.11 Optical bench disposition from left to right: laser, two absorptive filters, slit, CCD camera 39
3.12 Example of images obtained by the camera when the knob is at 3 mm, with 46.371 ms (top image) and 13.855 ms (bottom image) as exposure time 39
3.13 Diffraction figure with relative fitting, for knob at 0mm 41
3.14 HDR diffraction figure with relative fitting for knob at 3mm 41
3.15 Diffraction figure with relative fitting, for knob at 3mm 42
3.16 HDR diffraction figure with relative fitting for knob at 3mm 42
3.17 Diffraction figure with relative fitting, for knob at 5mm 43
3.18 HDR diffraction figure with relative fitting for knob at 5mm 43
3.19 Slit width calibration 44

Chapter 1

PLUS scientific objectives

In the field of Solar physics and exospheres' or atmospheres' studies, FUV/EUV imaging spectrometry has become essential, in fact there have been many missions which include a spectrometer in their payloads. Before continuing, the next paragraph illustrates a brief presentation of Mercury and Moon exospheres, that are the main possible applications of PLUS.

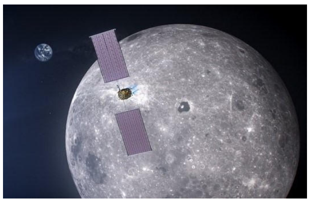

Figure 1.1: Moon's image

1.1 Science framework

The Moon and Mercury, contrary to other planets or satellites, are not surrounded by an atmosphere, but only by a surface-bounded exosphere, where atoms rarely collide, in fact each species can be thought as "independent atmospheres" [1].

Regarding the lunar exosphere, this is primarily made up of neutral atoms and molecules, which derive from the interaction with sun radiation, from radioactive decay and from meteoritic bombardment, balanced by losses into space and recycling back to the surface.
It was first observed by Apollo surface and orbital instruments in 1971, then through ground-based spectroscopic methods there was the discovery of sodium and potassium [1] and thanks to some missions to the Moon, also photo-ionized neutrals and secondary ions in the exosphere, including H_2+, He+, C+, Na+, O+, Al+, Si+, K+, CO+, Ar+, Fe+ and Ca+, have been detected [2].
Furthermore, using spectrometry in the 150-350 nm range to analyse the albedo both on the day side and the night side, gives the possibility to deepen our knowledge about the geological nature and composition of the surface and to support analysis for the search of iron-bearing silicate surfaces. For instance, pyroxenes, feldspars, olivines, and chondritic meteorites all exhibit a valuable "UV dropoff" in this range that is not seen in iron-bearing minerals (ilmenite, magnetite, ...).
Additionally, Moon surface albedo measurements can be obtained by push-broom scan of perenni-

ally shadowed craters or polar shadowed regions and can be useful to detect ice; on the night side they can also give information on H Ly-α sky-glow [3].

All these possible applications are summarised in the Figure below and they can be referred also to the study of Mercury. From the figure one can see that various aspects of the exosphere and the surface composition can be analysed while the instrument is orbiting.

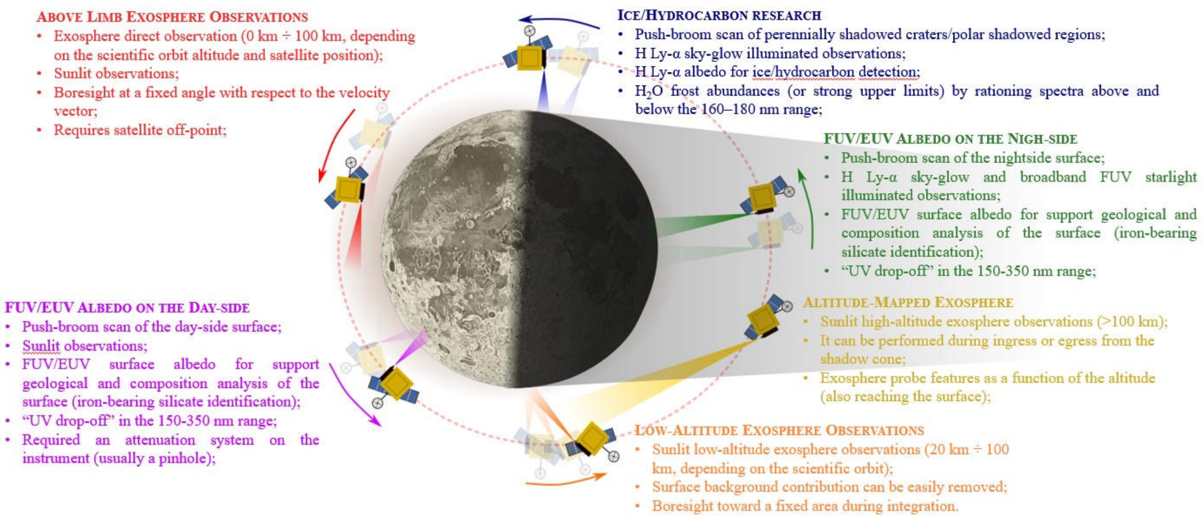

Figure 1.2: Possible observation modes

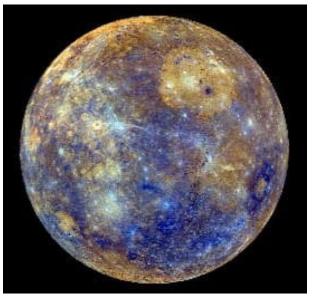

Figure 1.3: Mercury's image collage from MESSANGER spacecraft

As anticipated, Mercury does not have a proper atmosphere, but a thin layer of atoms and plasma, where gas molecules collide with the surface or escape from the planet rather than colliding with each other. The so-called Hermean exosphere is mainly composed of materials coming from Mercury's surface and solar wind, and of particles derived from impacts of comets and meteoroids. Its close proximity to the Sun creates particularly strong external forcing conditions, which contribute to the continuous reconfiguration of the exosphere, that is refilled and eroded through a variety of chemical and physical processes, making it highly dynamic.

Hermean exosphere was first detected by Mariner 10 during its three flybys (1974-1975), it observed emissions from hydrogen (H) and helium (He) atoms respectively at 121.6 nm and 58.4 nm and from oxygen at 130.4 nm [4], it also discovered Mercury's unexpected magnetic field. Later, thanks to ground-based telescopes, it was possible to detect three other species: atomic sodium, potassium, and calcium from emission lines in the visible range [4]; MESSENGER (MErcury Surface, Space ENvironment, GEochemistry and Ranging) in 2009 also discovered magnesium during its second flyby, and detect calcium ions, atomic manganese and aluminium afterwards. The knowledge of the dynamics and composition of Mercury exosphere and magnetosphere is expected to improve significantly with the Bepi-Colombo mission (described in paragraph 1.2), since it allows simultaneous two-point measurements thanks to two spacecrafts and an accurate spectrum analysis due to the splitting of the range in far and extreme ultraviolet.

The use of UV spectrometers, together with in-situ measurements, has been fundamental to discover everything we know about Moon's and Mercury's exosphere. Today's challenge is to push forward this technology with new enhanced components and design, this is the aim of the PLUS project.

Spectrometers are based on spectroscopy theory, that is the study of absorption and emission of light and other radiation by matter. It involves the splitting of electromagnetic radiation interacting with a sample into its constituent wavelengths, i.e., the spectrum. From this, it is possible to detect constituents of a sample, since every element has a unique light spectrum.

Figure 1.4 shows an example of a spectrum [5] gained with PHEBUS, the most recent FUV/EUV spectrometer on a space mission. The example represents the results obtained with Argon gas using the zero-order position of the monochromator to record the full spectrum between 55-155 nm. Data were processed by numerical computing software which displayed the real image seen by the detector (Figure 1.4a) and plotted the relative spectrum (Figure 1.4b).

Please note that the x-axes has been calibrated knowing the Argon theoretical emission lines, thus, the pixel values has been replaced by the wavelength values.

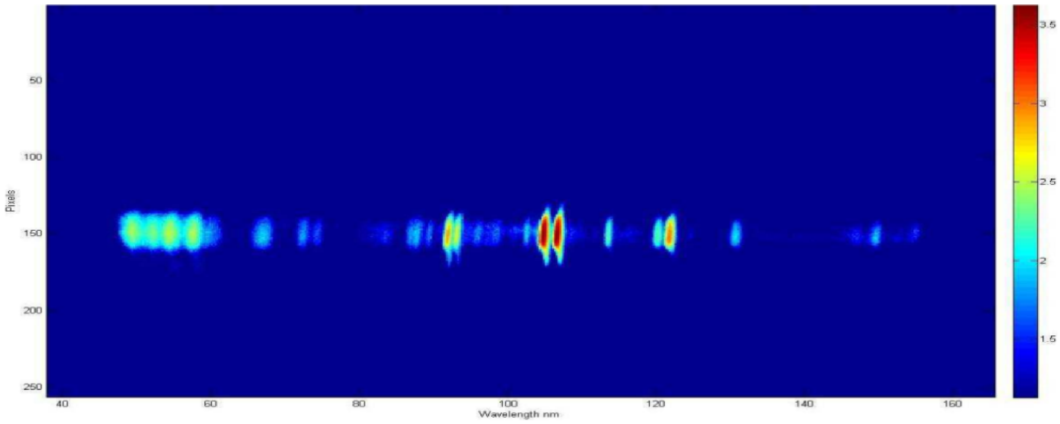

(a) EUV detector Image with cumulated integration time of 10 min and count rate of 1500 cps

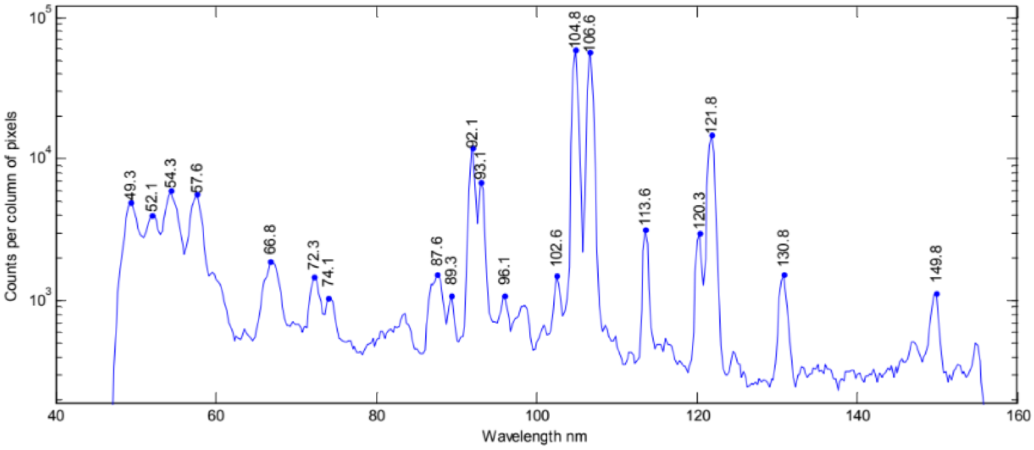

(b) EUV spectrum from the image Fig.1.4a

Figure 1.4: EUV detector image and spectrum for Argon gas: HV=-3436 V [5]
(Levels are in log_{10}-scale)

One can easily identify from Figure 2.5 that at 104.8 & 106.6 nm (Ar I) and at 92.0 & 93.2 nm (Ar II) there are two peaks, these represent two characteristic Argon doublets. It is also possible to observe other lines maybe due to contamination such as H I at 121.6 nm, then, the lines seen at 113.6 nm seems to be N I triplet around 113.4 nm, and the one read at 130.8 nm seems to be O I triplet around 130.4 nm [5]. This example shows how the spectrum can be useful for example to understand the composition of the atmosphere or exosphere of planets/satellites, that is PLUS main application. Spectroscopic observation in the far and extreme ultraviolet spectral region is a valuable technique also for other interesting purposes, for instance [6]:

- Investigate auroras occurring in giant planets, in fact the 50-200 nm range covers all the important features related to the H_2 bands and the H Lyman series produced in auroras, as well as some important signatures of aurora-produced hydrocarbons.

- Retrieve information on solar wind-magnetosphere-ionosphere interactions through observations of other ionized species signatures and in-situ measurements of the magnetic field.

- Study giant planets ring systems, giving valuable information on the composition, structure and spatial dimensions.

- Detect ice through surface albedo measurements looking for HO, H_2O, S_2O.

- Gain information on the geological nature and composition of the planetary surface.

- Observe gas or ice giant planets (Europa, Titan, Triton, . . .) or the inner planets.

1.2 Background

PLUS is the last FUV/EUV imaging spectrometer on which scientists are working; before it, there have been many others, some important examples are listed below:

- Alice on Rosetta (2004-2016) and New Horizon (2006-still going) spacecrafts, it allows to analyse gases in the coma and tail and to measure the comet's production rates of water and carbon monoxide/dioxide; It also provides information on the surface composition of the nucleus [7];

- Lyman-Alpha Mapping Project (LAMP), a Lunar Reconnaissance Orbiter LRO (2009-still going) instrument which searches for surface ice and frost in the lunar polar regions and provide images of permanently shadowed regions illuminated only by starlight and the glow of interplanetary hydrogen emission, the Lyman-Alpha line [8];

- UVS (Ultraviolet spectrograph) on board Juno (2011-still going) aims to sense Jupiter's auroral morphology and brightness and to map the mean energy and flux of precipitating auroral particles [9];

- SPICAV (Spectroscopy for the investigation of the characteristics of the atmosphere of Venus), it consists in three spectrometers in the UV and IR range flying on the Venus Express VEX (2005-2014) orbiter and it is dedicated to the study of the atmosphere of Venus from ground level to the outermost hydrogen corona [10].

Each of these instruments is based on a proper optical scheme in order to optimise their performances. Except for SPICAV, the others use a standard Rowland configuration with only one optical surface and a detector having a cylindrically-curved MCP-stack that matches the Rowland circle.

Though, the most recent spectrometer launched on a space mission is PHEBUS (Probing of Hermean Exosphere By Ultraviolet Spectroscopy), which is a French-led two-channels spectrometer developed as a cooperative project involving Japan, Russia and Italy (who provided ground facilities for calibration in the vacuum ultraviolet). It is one of the instruments useful to characterise the exosphere, magnetosphere and surface of Mercury and better understand their interaction.

The following table illustrates a comparison between some of the main features of the mentioned spectrometers.

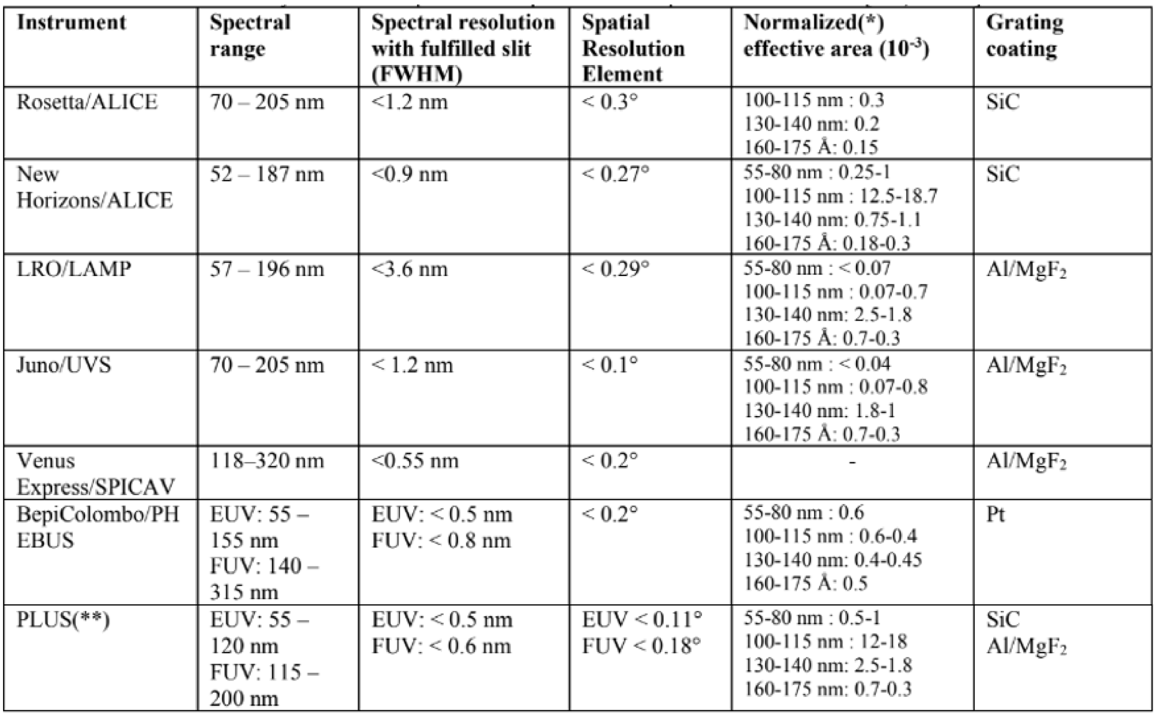

Instrument	Spectral range	Spectral resolution with fulfilled slit (FWHM)	Spatial Resolution Element	Normalized(*) effective area (10^{-3})	Grating coating
Rosetta/ALICE	70 – 205 nm	<1.2 nm	< 0.3°	100-115 nm : 0.3 130-140 nm: 0.2 160-175 Å: 0.15	SiC
New Horizons/ALICE	52 – 187 nm	<0.9 nm	< 0.27°	55-80 nm : 0.25-1 100-115 nm : 12.5-18.7 130-140 nm: 0.75-1.1 160-175 Å: 0.18-0.3	SiC
LRO/LAMP	57 – 196 nm	<3.6 nm	< 0.29°	55-80 nm : < 0.07 100-115 nm : 0.07-0.7 130-140 nm: 2.5-1.8 160-175 Å: 0.7-0.3	Al/MgF_2
Juno/UVS	70 – 205 nm	< 1.2 nm	< 0.1°	55-80 nm : < 0.04 100-115 nm : 0.07-0.8 130-140 nm: 1.8-1 160-175 Å: 0.7-0.3	Al/MgF_2
Venus Express/SPICAV	118–320 nm	<0.55 nm	< 0.2°	-	Al/MgF_2
BepiColombo/PHEBUS	EUV: 55 – 155 nm FUV: 140 – 315 nm	EUV: < 0.5 nm FUV: < 0.8 nm	< 0.2°	55-80 nm : 0.6 100-115 nm : 0.6-0.4 130-140 nm: 0.4-0.45 160-175 Å: 0.5	Pt
PLUS(**)	EUV: 55 – 120 nm FUV: 115 – 200 nm	EUV: < 0.5 nm FUV: < 0.6 nm	EUV < 0.11° FUV < 0.18°	55-80 nm : 0.5-1 100-115 nm : 12-18 130-140 nm: 2.5-1.8 160-175 nm: 0.7-0.3	SiC Al/MgF_2

Figure 1.5: Summary of the main spectrometer parameters [6]

PHEBUS has been the first spectrometer to split the range into the far and extreme ultraviolet spectral range. PLUS follows this same approach, contrary to the previous spectrometers which had just one channel. Since they had only one channel, their design was simpler than the one of PHEBUS or PLUS, though the width of their spectral range did not allow to optimise the optical efficiency.

PHEBUS- is composed of two blocks, the collecting and the spectrometer parts. The former includes the straylight rejection baffle, the primary mirror (accomodated inside a scanner rotating mechanism), and the entrance slit; the latter consists of two channels (EUV and FUV channel) and four different detectors, which cover the spectral range 55-315 nm and two additional narrow windows at 404 nm and 422 nm (NUV Ca and NUV K).
The inner view of the instrument is shown in the Figure 1.6 on the side. The light enters in the baffle and is focused to the slit by a parabolic mirror; then, it is diffracted by two holographic

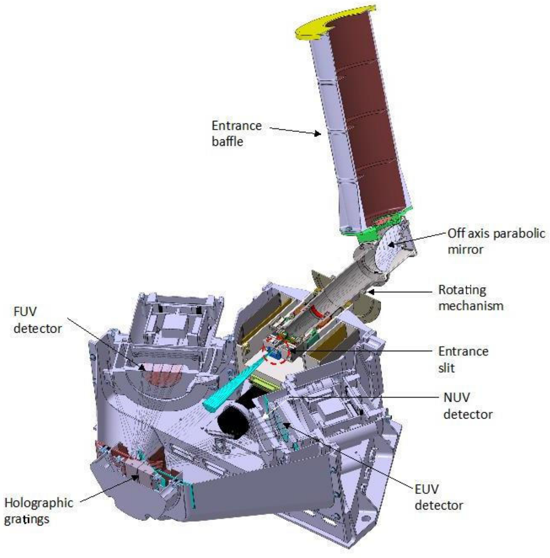

Figure 1.6: PHEBUS inner view [11]

gratings and collected by two Multi Channel Plates (MCPs) detectors, which return the spectra in the two spectral ranges. The light diffracted by the FUV grating is also measured by the two NUV channels thanks to the use of two mirrors positioned in the correct spot. Figure 1.7 below displays the optical layout just described.

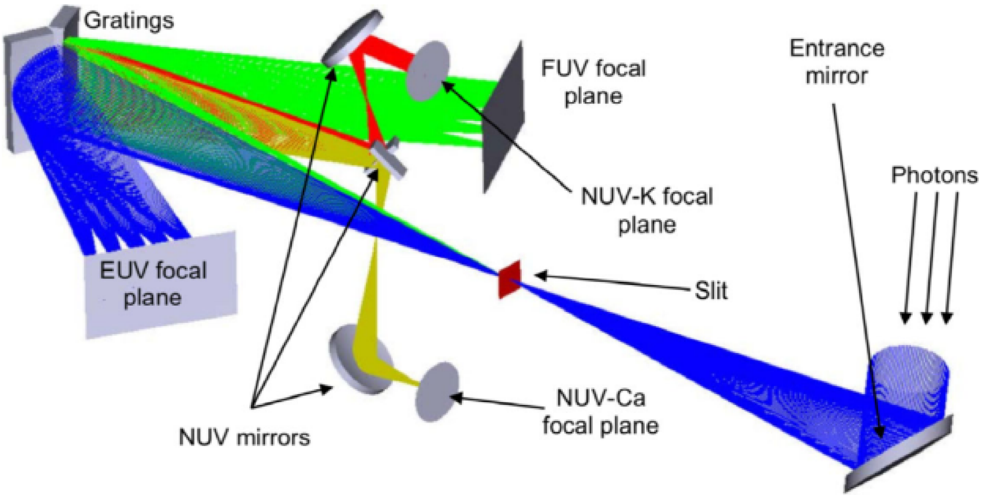

Figure 1.7: PHEBUS optical layout [4]

PHEBUS is now on board Bepi-Colombo mission, which is the fifth Cornerstone mission of the Horizon 2000+ mission adopted by the ESA SPC in 2007 for the Scientific Directorate programme; it is a European Space Agency (ESA) - Japan Aerospace eXploration Agency (JAXA) collaboration dedicated to the study of Mercury (from the inner structure to the environment). The aim of the Bepi-Colombo mission is to investigate the Hermean exosphere (its composition, dynamics, and its interactions with the surface), the magnetosphere, and the solar wind, which strongly influences the surface and the exosphere. It was launched in October 2018 and it is composed by two spacecrafts, the Europe-led Mercury Planetary Orbiter (MPO), where PHEBUS is flying, and the Japan-led Mercury Magnetospheric Orbiter (MMO); they will operate autonomously once reached the orbit of Mercury in December 2025 [12].

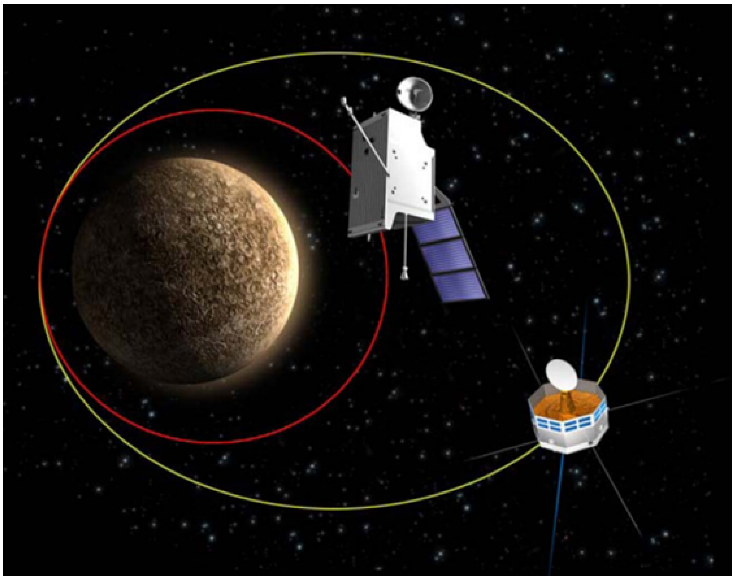

Figure 1.8: The MPO and MMO in Mercury orbit [13]

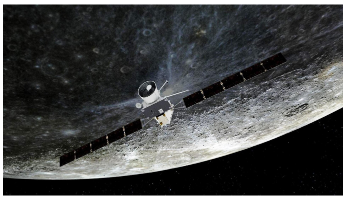

Figure 1.9: 1st Bepi-Colombo Mercury flyby in 2021

During the long cruise to Mercury, Bepi-Colombo will perform nine flybys in total: it has already been in proximity of the Earth in 2020 and of Venus both in 2020 and 2021, it has also accomplished two Mercury flybys in 2021 and 2022 (23rd June) and it is expected to fly again near the planet four other times, before inserting on its orbit on 5th December 2025. The primary purpose of the flybys is to use Mercury's gravity to fine-tune Bepi-Colombo's trajectory. Moreover, during the 2nd Mercury flyby a sequence of snapshots has been taken by three cameras showing the planet's surface, while some monitoring instruments have sampled the environment from both near and far from the planet in the hours around close approach.

Before Bepi-Colombo mission, there has been another important mission which investigated Mercury's chemical composition, geology, and magnetic field: MESSENGER (MErcury Surface, Space ENvironment, GEochemistry and Ranging), which represents PHEBUS' precursor.

It is the second mission, after Mariner 10 in 1975, to reach Mercury; it was launched on 3rd August 2004, only on 17th March 2011 it entered into Mercury orbit and remained there until the end of the mission on 30th April 2015.

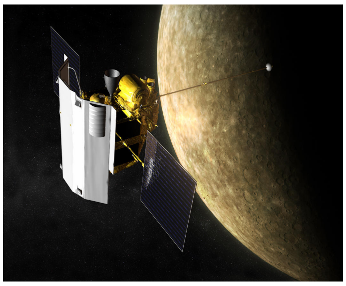

Figure 1.10: MESSENGER in Mercury orbit

MESSENGER's payload was composed of:

- Mercury Dual Imaging System (MDIS), able to map landforms, track variations in surface spectra and gather topographic information.
- Gamma-Ray and Neutron Spectrometer (GRNS) detects gamma rays and neutrons that are emitted by radioactive elements on Mercury's surface or by surface elements that have been stimulated by cosmic rays.
- Magnetometer (MAG), maps Mercury's magnetic field and searches for regions of magnetized rocks in the crust.
- Mercury Laser Altimeter (MLA), it can measure the amount of time for light to make a round-trip to the surface and back in order to produce highly accurate descriptions of Mercury's topography.
- Mercury Atmospheric and Surface Composition Spectrometer (MASCS), it is sensitive to light from the infrared to the ultraviolet; it can measure the abundances of atmospheric gases and detect minerals on the surface.
- Energetic Particle and Plasma Spectrometer (EPPS) measures the composition, distribution, and energy of charged particles (electrons and various ions) in Mercury's magnetosphere.
- Radio Science (RS) measures very slight changes in the spacecraft's velocity through the Doppler effect.

All these instruments have been necessary in the study of Mercury, in particular during the flight towards Mercury, MESSENGER accomplished three Mercury flybys, from which it observed the previously detected species H, Na, and Ca; it also detected new species, such as magnesium, calcium ions, atomic manganese and aluminium. Surprisingly, it did not observed emissions from O, detected by Mariner 10 with a lower sensitivity, and it did not identified the potassium line at 404 nm, even though it was observed from Earth. Once MESSENGER reached Mercury orbit, it regularly observed calcium, sodium and magnesium in the exosphere and understood their distribution in the exosphere.

1.3 Scope of PLUS

PLUS is a multichannel EUV (40-115 nm)/FUV (115-200 nm) imaging spectrometer working in the 55-200 nm with a potential third channel at longer wavelength (up to 350 nm) [3]. It returns two spectra, in the EUV and FUV range, from these it is possible to determine the exosphere composition and dynamics of planets or satellites acting as shield against the scattered solar light. Then, the analysis can be further confirmed through in-situ measurements, in fact both in-situ and remote observations are needed. The first give very precise measurements of the composition, chemistry, dynamics and evolution, though it is spatially and temporally limited; conversely, the last allow a great spatial coverage, a valuable temporal analysis and the concentration measurements of a broad set of constituents undetectable with in-situ techniques.

The main scientific objectives of PLUS can be summarized as follows:

- Determine the exosphere composition and dynamics of planets or satellites.
- Probe the lunar exosphere, since the most significant spectral features are in the 55 to 350 nm spectral range, where neutral atoms and relative ions ($N, H, He, C, O, S, \dots$), molecules (CO, H_2, OH..) and hydrocarbons (CH_4, C_2H_2, C_2H_4, C_2H_6, HCN, $HC3N$,$\dots$) can be detected [3].
- Give additional information on the geological nature and composition of the surface by analysing the albedo in the range 150-350 nm, this also support the analysis for the search of iron-bearing silicate surfaces.
- Detect ice, which can be performed by push-broom scan of perennially shadowed craters or polar shadowed regions.

Among these, one interesting application of PLUS is to use it in order to analyse the lunar exosphere, it is possible to obtain a probe of the exosphere features as a function of the altitude and to perform direct observations of the exospheric emission pointing the field of view at different heights.

Another possibility is that PLUS will follow PHEBUS' footsteps and explore Mercury. Figure 1.2 of paragraph 1.1 illustrates the possible scenarios in which the instrument can be while orbiting around a planet or satellite.

Compared to PHEBUS, PLUS will show improved performance by using highly efficient optical components optimized for each channel and high resolution and dynamic range solar blind photon counting detectors. This is possible because of the split of the spectral range into two channels, which grants a precise spectral analysis and improves the throughput of the instrument, thus its S/N ratio capabilities increase. Then, thanks to novel MCP detectors based on a 2D anode array integrated into imaging Read Out Integrated Circuits (MIRA - MIcrochannel plate Readout ASIC), with photon counting capability on chip, the spatial resolution will grow, as well as the lifetime of the detectors. PLUS' optical design and components are deeply described in the next Chapter.

Chapter 2

Instrument description

PLUS, as has been said earlier, is a novel dual channel FUV/EUV imaging spectrometer working in 55-200 nm spectral range with a potential third channel at longer wavelength (up to 350 nm) [3]. PLUS can be mainly used to study exosphere composition and dynamics of planets or satellites by the analysis of the returned spectrum. Additionally, it could also become useful in solar and space weather physics instrumentation.

The aim of the project is to realise a spectrometer characterised by improved detection limit, shorter observations integration time and higher dynamic range. This will be achieved thanks to high efficient optical components and to solar blind photon counting detectors with high spatial resolution and dynamic range. This last feature is important since, once the detector integration time is defined, the improvement of the dynamic range allows to observe more faint features which would otherwise be impossible to distinguish from the noise background. The detector is expected to have spatial resolution close to 30 μm and exceptional performance in terms of dynamic range (count rate $>$ 10 Kcounts/pixel/s). This will allow to measure, simultaneously and without the necessity of filters, spectral lines with different intensities of orders of magnitude, exploiting the maximum Signal to Noise Ratio provided by the statistical limit.

2.1 Optical scheme

PLUS implements a compact and simplified scheme compared to PHEBUS, in fact it is based on the Harada configuration, in which a specific out-of-Roland geometry guarantees improved performances and an optimised aberration compensation making use of two spherical variable-line-spaced gratings [14]. Its optical design has been realised using Zemax software.

Figure 2.1 illustrates the scheme of PLUS optical design: the light enters into the slit S, which diffracts it for the first time, introducing an initial spectral components separation; the principle behind it is deeply described in paragraph 3.2.1 of Chapter 3, where there is also the slit's picture (Figure 3.8). Then, the light is reflected by two variable line-spaced (VLS) gratings G1 and G2, which further separate the wavelengths within the EUV and FUV spectral ranges. Finally, two detectors D1 and D2, one for each channel, collect the diffracted light and count the amount of photons for each pixel, realising the two spectra.
Splitting the range into two channels guarantees an accurate spectral analysis and high efficient optical components for each channel, these are described in the next paragraphs.

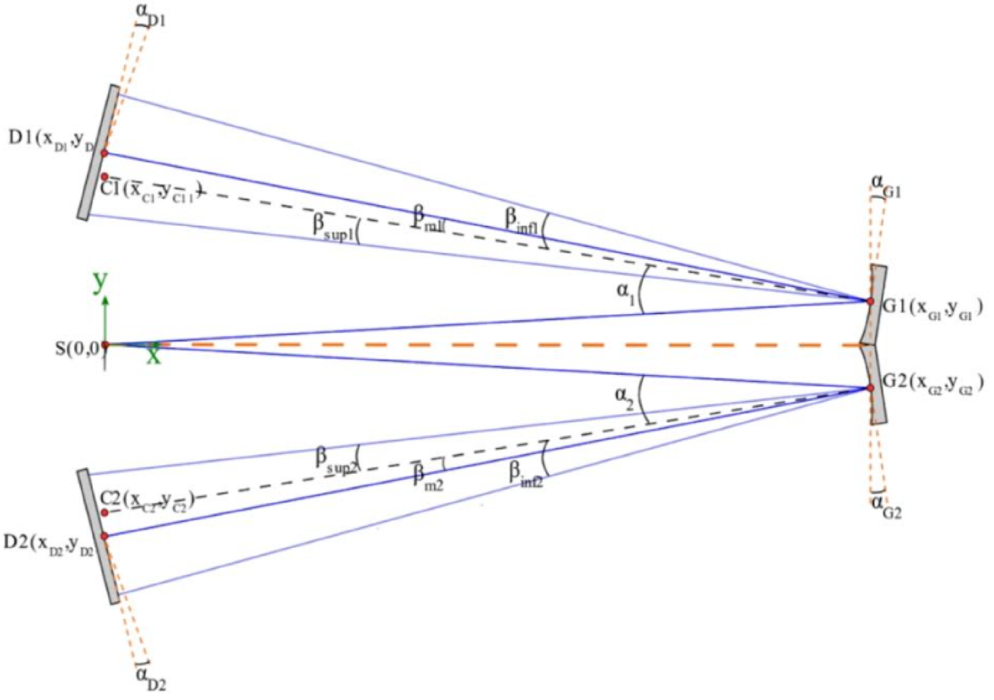

Figure 2.1: PLUS optical layout [15]

The following table reports the parameters of the two channels:

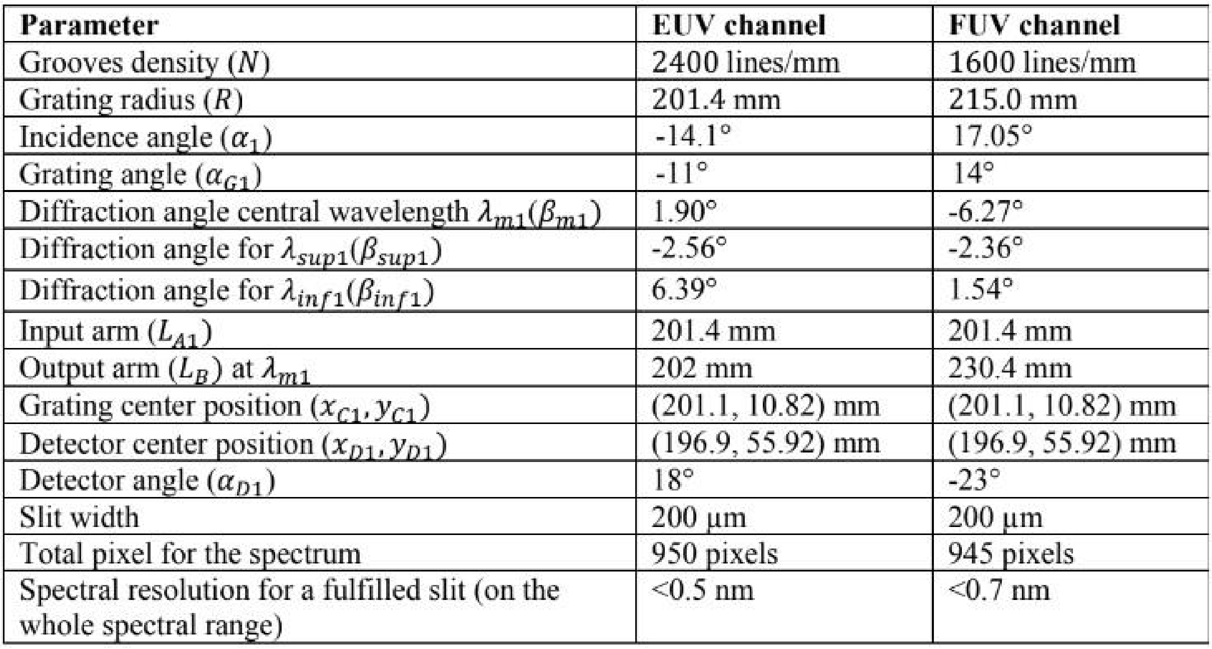

Parameter	**EUV channel**	**FUV channel**
Grooves density (N)	2400 lines/mm	1600 lines/mm
Grating radius (R)	201.4 mm	215.0 mm
Incidence angle (α_1)	-14.1°	17.05°
Grating angle (α_{G1})	-11°	14°
Diffraction angle central wavelength $\lambda_{m1}(\beta_{m1})$	1.90°	-6.27°
Diffraction angle for $\lambda_{sup1}(\beta_{sup1})$	-2.56°	-2.36°
Diffraction angle for $\lambda_{inf1}(\beta_{inf1})$	6.39°	1.54°
Input arm (L_{A1})	201.4 mm	201.4 mm
Output arm (L_B) at λ_{m1}	202 mm	230.4 mm
Grating center position (x_{C1}, y_{C1})	(201.1, 10.82) mm	(201.1, 10.82) mm
Detector center position (x_{D1}, y_{D1})	(196.9, 55.92) mm	(196.9, 55.92) mm
Detector angle (α_{D1})	18°	-23°
Slit width	200 µm	200 µm
Total pixel for the spectrum	950 pixels	945 pixels
Spectral resolution for a fulfilled slit (on the whole spectral range)	<0.5 nm	<0.7 nm

Figure 2.2: PLUS optical configuration parameters [15]

2.2 Grating Components

Each channel is equipped with novel coatings having high efficiency in the specific restricted wavelength range, thanks to the split of the spectral range.
The prototypes of the gratings including the deposition of SiC and Al/MgF_2, have already been fabricated, they are displayed in Figure 2.3 and 2.4.

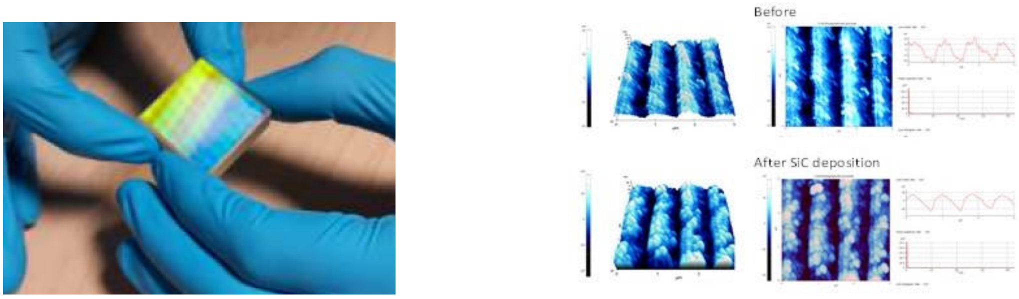

Figure 2.3: EUV channel SiC plane grating prototype with SiC thickness of 70 nm and 1200 lines/mm [6]

Figure 2.4: FUV channel Al/MgF_2 plane grating prototype with $Al/MgF_2 + Cr$ thickness of 75 nm [6]

The development of the coatings has been carried out using the deposition facilities available at the CNR-IFN. E-beam/thermal evaporation has been employed for Al coating for the FUV channel, whereas the RF-magnetron sputtering has been employed for the carbon-based coating, which has high reflectance in the EUV spectral range.
The grooves profiles, visible in the figures above, have been obtained using atomic force microscope (AFM). From them one can notice that after the deposition, the profiles have remained almost the same, this is important in order to keep the performance and operation of the original gratings. In this way the efficiency of the optics in the FUV channel is expected to double and the EUV channel is expected to achieve an improvement of 15-20%, with respect to the conventional solutions [14].

2.3 Detectors

As a result of the PLUS components alignment visible in Figure 2.1, each detector is able to collect UV rays in the relative spectral range (FUV/EUV). The detectors are Micro-Channel Plates (MCPs) on a 2D anode array, integrated into imaging Read Out Integrated Circuits (MIRA – Micro-channel plate Readout ASIC), with photon counting capability on chip.

MCPs have been the detectors of choice for astronomical applications in FUV/EUV for a long time, in fact they can provide very high time resolution (down to 10ps), high spatial resolution (down to $\sim 10\mu m$), large format arrays ($>$ 1K x 1Kpixels), large sensitive area size (up to 20 cm), photon counting capability with virtual zero noise, possibility of optimizing the efficiency in a given range of wavelength with appropriate photocathode choice, with high out of band rejection, radiation hardness and operation at room temperature. Moreover, there have been recent developments in the production of MCPs which provide significant improvements in the lifetime and in the stability of these devices. MCP aging depends on the extracted charge (the total number of electrons produced for secondary emission), in the past it produced a sensible effect on the performance when the it was an order value of fraction of C/cm^2; while on new devices there should be no degradation even up to 10 C/cm^2, thanks to the lower gain [16].
For this reason, the readout system need not to limit the MCPs intrinsic dynamics and shall allow operations with the lowest possible gain. The one proposed for PLUS is MIRA ASIC, which also guarantees unprecedented performance in terms of dynamic range combined with spatial resolution close to 30 μm.

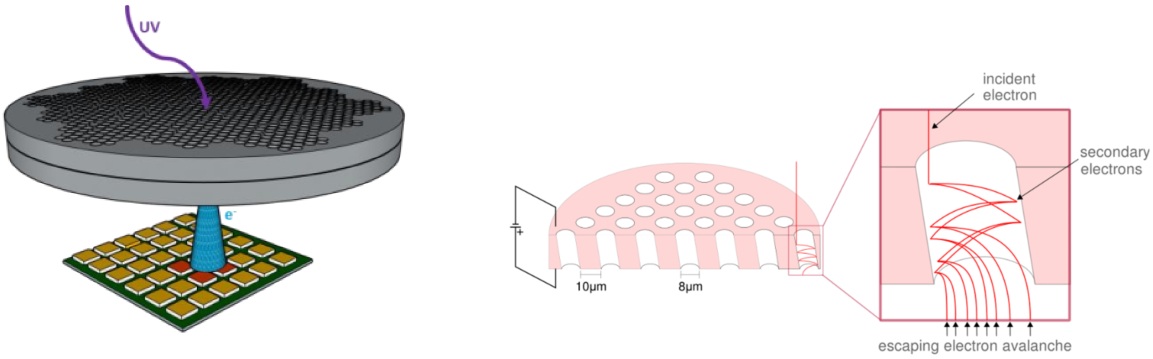

(a) Photocathode and MCP to convert the UV radiation into electrons, MIRA to collect the charge cloud and count the incoming events [17]

(b) MCP operating principle

Figure 2.5: The PLUS detector

Figure 2.5a above displays the basics of the detector operating principle: The UV radiation hits the photocathode giving the electrons the energy to come out of the surface based on the photoelectric effect; these electrons are subjected to a potential and attracted towards the 2D anode array where the Micro-Channel Plate is placed. An MCP is a slab made from resistive material (most often glass) with an array of tiny tubes (microchannels) oriented parallel to one another, it exploits secondary emission to multiply the incident electrons. This is possible because of an angle between the plate and the microchannels, hence the electrons that enter in one of the channels are guaranteed to hit the wall and a cascade of electrons is generated and propagated through the channel (see Figure 2.5b) resulting in electron multiplication factors of 10^4-10^7.

After the photons have been converted in electrons and these have been multiplied, MIRA ASIC (see Figure 2.6) detects the cloud of electrons generated by each photon and reads out the pixels in order to obtain the spectrum. As has been said earlier, MIRA's design allows to exploit all the advantages of the improved performance of new MCPs, for example it reduces the input Equivalent Noise Charge (ENC), allowing operations with lower MCP gain.

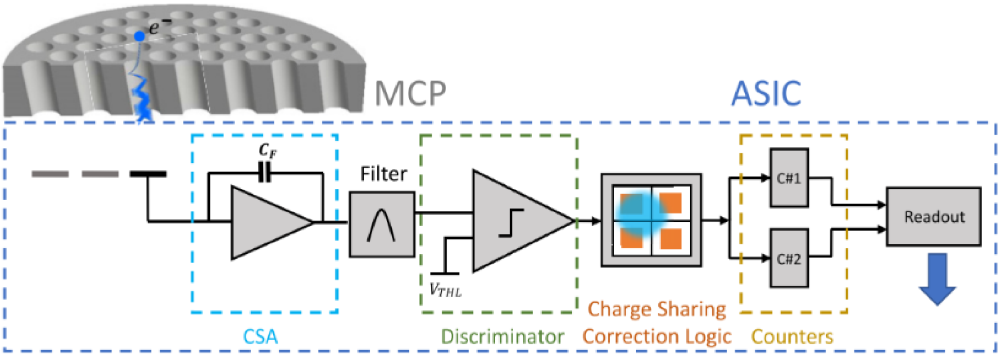

Figure 2.6: Pixel readout chain of MIRA ASIC [17]

Looking at Figure 2.6 one can see that each pixel contains an anode to collect the electrons emitted by the MCP, a low noise Charge sensitive amplifier (CSA) and a filter to maximize the SNR, a comparator to recognize and count single photon events, logic to correct for charge sharing among pixels (CSCL), and two counters [15].

The Charge Sharing Correction Logic is particularly important because the diameter of the electron cloud is comparable with the pixel pitch of 35 μm, thus the charge sharing effect is highly likely to occur in a cluster of 4 pixels. Hence, CSCL assigns the count to the pixel with the highest amount of collected charge by comparing the discriminator outputs of different pixels.
The ASIC features three modalities of Charge Sharing Correction Logic: Mode 1, for testing purposes, where the pixel is configured in Single Pixel mode and the Charge Sharing Correction Logic

is disabled, Mode 2 where the pixel is configured in Single Pixel mode and the Charge Sharing Correction Logic performs horizontal and vertical comparisons, and Mode 3 where the pixel is configured in Charge Summing mode: the cluster with the highest amount of charge is selected and the pixel, inside the cluster, with the highest amount of charge is identified.
The presence of the CSCL is also needed to grant a spatial resolution limited to the pixel size, for this reason MIRA has a compact pixel size (35μm x 35μm) for a total of 32x32 pixels in a 2mm x 2mm ASIC area, this allows to have low noise, high count rate and high spatial resolution.

Another fundamental feature of MIRA is that each pixel hosts 2 counters, at each time one will be used to count photons and the other will be available to be readout in order to achieve zero dead time. This is possible because the counters are implemented as Linear Feedback Shift Register, thus, they are able to work as a counter or a shift register alternatively. Pixel's readout is actually very efficient, in fact all pixels are readout within 1s time, scanning each pixel in the array in a regular way.
To sum up, the main characteristics achievable with MIRA are listed: reduction of the input Equivalent Noise Charge, count rate per pixel of 100 kcps, spatial resolution of 35μm, low noise and zero dead time [17]. Once the electrons for each pixel have been counted, it is finally possible to visualize the sprectrum, as shown in Figure 1.4 of Chapter 1.

2.4 The system and the EUV channel demonstrator

The whole spectrometer model is shown is Figure 2.7, it puts together the components described in the previous paragraphs.

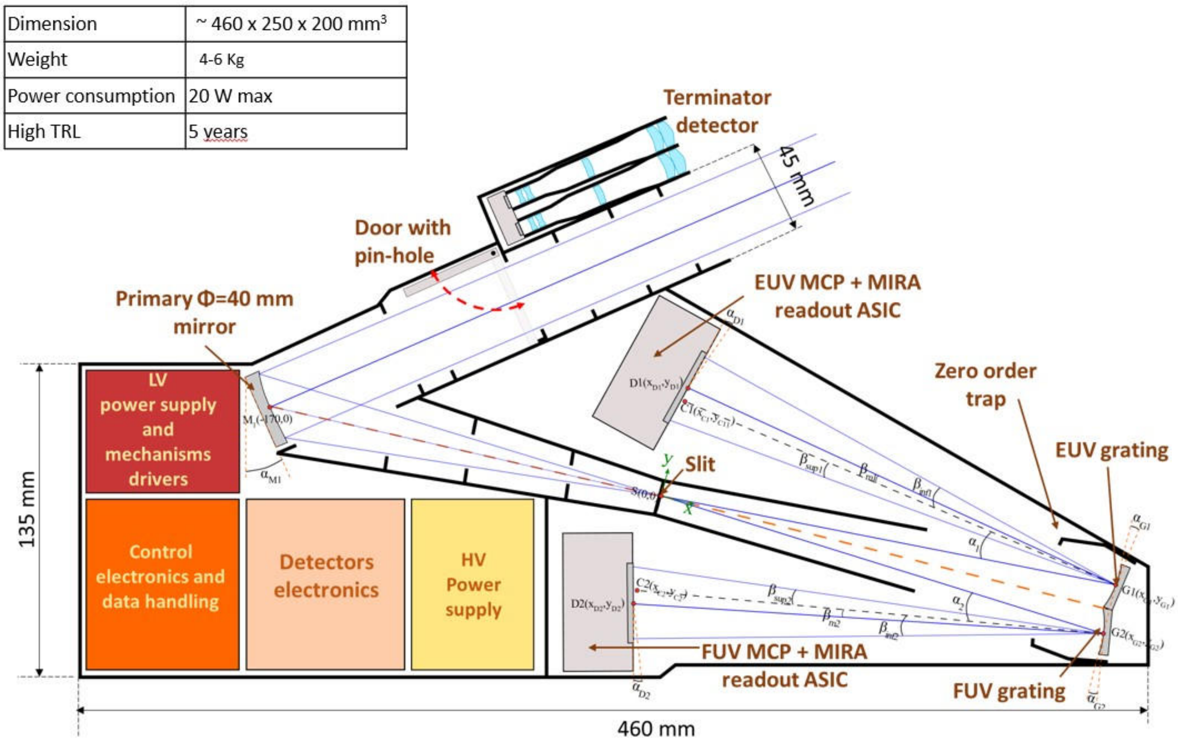

Dimension	~ 460 x 250 x 200 mm^3
Weight	4-6 Kg
Power consumption	20 W max
High TRL	5 years

Figure 2.7: PLUS Opto-mechanical concept

Currently, a demonstrator of the EUV channel is under realization (see Paragraph 2.4 of Chapter 2) in order to test the performances, thus it is necessary to be in the most similar conditions in which the instrument will work. For this reason, the instrument will be tested in cleanroom inside a vacuum chamber, in particular, it will be implemented in the ISO7 clean-room of the CNR-IFN, where the optical system (composed by a slit, two optical gratings, one single detector optimized for the EUV channel) will be aligned on a vacuum-compatible breadboard [14].

The vacuum chamber and the grating's supports that will be used for the EUV channel demo are displayed in Figure 2.8.

From Figure 2.9 one can see that the vacuum chamber has two entries, one where the slit has already been placed and one where there will be the EUV detector.

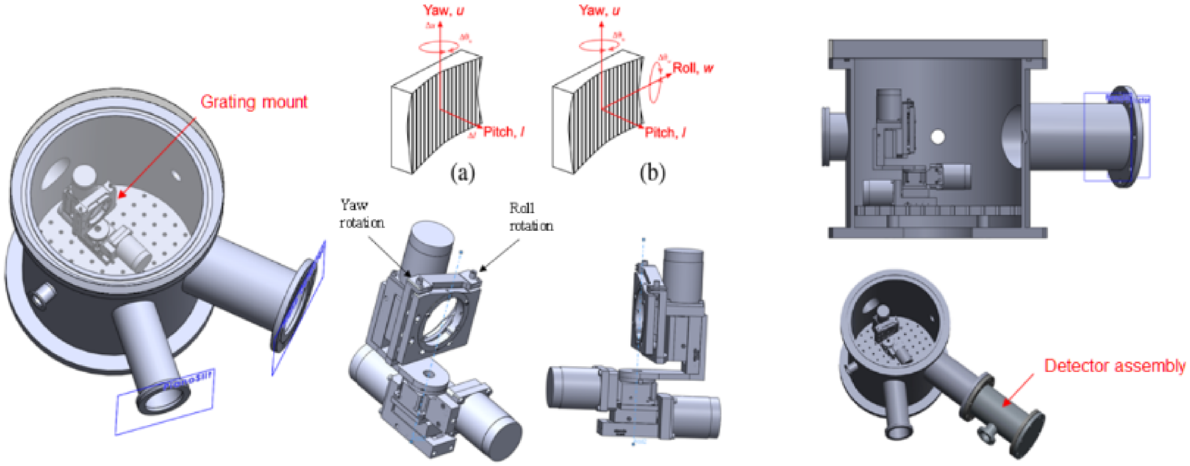

Figure 2.8: Opto-mechanical parts for the EUV channel demo realisation [6]

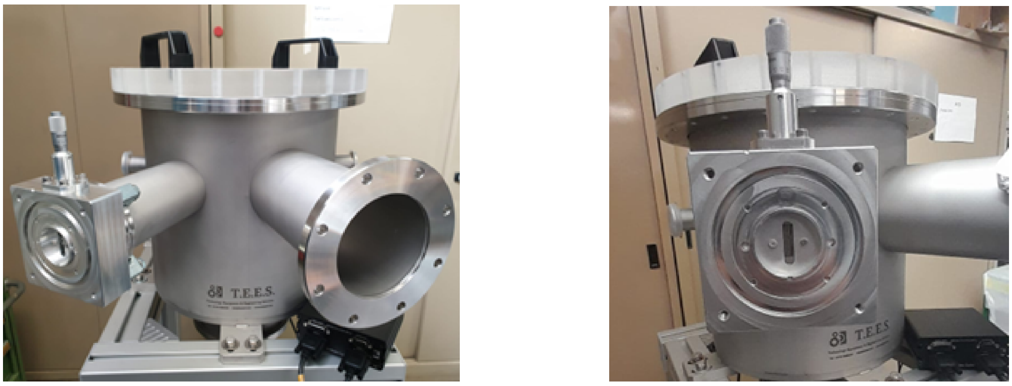

Figure 2.9: Picture of vacuum chamber for the EUV channel demo realisation

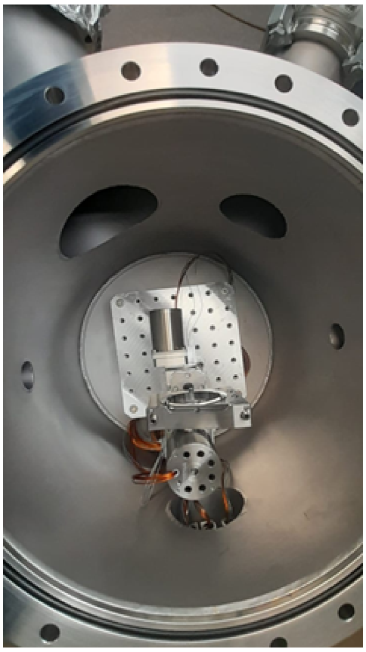

Figure 2.10: Picture of the inside of the vacuum chamber

Inside the vacuum chamber, the vacuum compatible gratings' mounts are positioned (Figure 2.10); they can be aligned as desired using a specific software, which is described in paragraph 3.1 of Chapter 3.

Furthermore, at the moment the prototypes of the gratings are ready, they are visible in Figures 2.3 and 2.4; and the detector prototype is under development. The detector is composed of a Chevron stack of two matching MCPs (in contact, with no gap in between), which characteristics are available in [16], and of the MIRA ASIC demonstrator, which has been designed to fulfill the following main requirements:

- Small pixel: 35 μm, to allow compact optical layout of the instrument.
- High maximum count rate: 100,000 counts/pixel/s.
- Negligible dead time.
- Low noise: ENC $<$ 50 e-, which allows to use low gain MCPs.
- Moderate time resolution (1s).
- Correction for charge sharing among pixels.
- 3 operative modes: one for testing purposes and two with different methods for event detection and charge sharing correction. [16]

The prototypes of the detector and the MIRA ASIC have been fabricated and assembled. The figures below show the relative pictures:

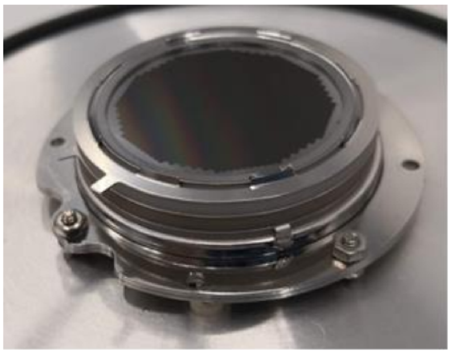

Figure 2.11: MCP Chevron assembly [16]

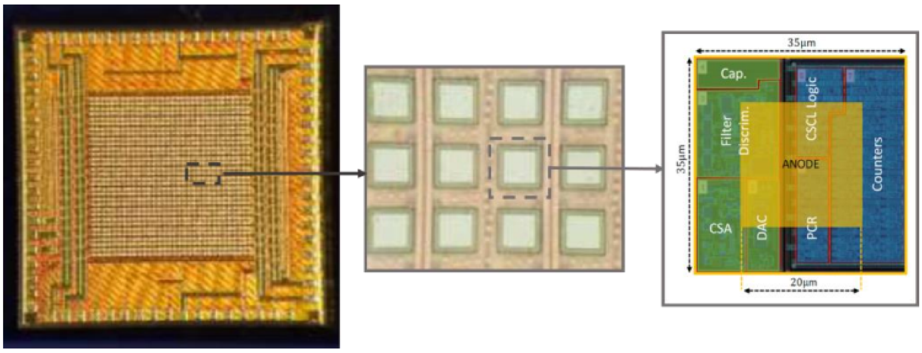

Figure 2.12: MIRA first release with a zoom view of the pixel structure [16]

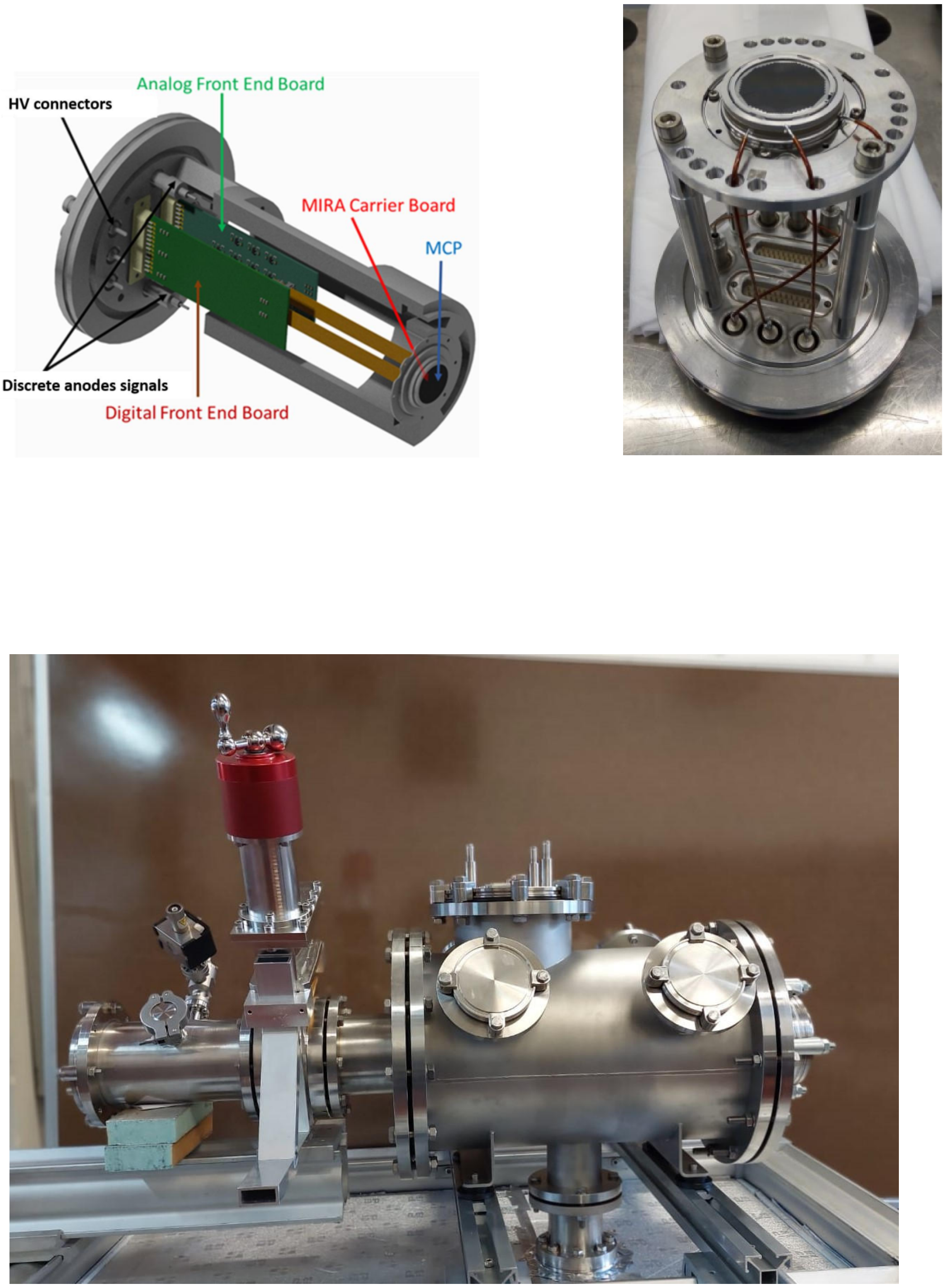

Figure 2.13: Detector prototype assembly [16]

Chapter 3

Experimental activities

The present chapter describes two laboratory activities, performed by the author in May-June 2022, these activities are preliminary to the realisation of the EUV channel demonstrator, which is expected to prove the resolution and the high efficiency of the system. They consist in: starting up the gratings' mounts controller and understand how to move these supports in order to realise the desired alignment; and in calibrating the slit width by analysing the diffraction figure when the slit is illuminated by a laser beam.

3.1 XILab software

The gratings will be positioned on specific vacuum compatible stages available on Standa website and visible in Figure 3.2. They have two possible rotations' axes, roll and yaw, and a translation axis, pitch. These terms in general indicate three axes around which an object could rotate as illustrated in the Figure on the side.

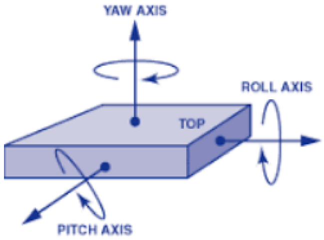

Figure 3.1: Rotations' axes

(a) STANDA Mod.8MR174V-11-VSS42 MOTORISED ROTATION STAGE (b) STANDA Mod. 8MT173V-10-VVSS42 MOTORISED TRANSLATION STAGE

Figure 3.2: Standa motorised stages used inside the vacuum chamber

The stages can be controlled using the 8SMC5-USB - Stepper & DC Motor Controller [18] shown in Figure 3.3 on the side. This controller is able to drive both stepper and DC motors and it is compatible with all the Standa stages; it can be connected to the PC via USB ports and can be used through the XILab software, which is especially designed for stages control, diagnostic and fine tuning of the motors driven by the controllers.

Figure 3.3: 8SMC5-USB - Stepper & DC Motor Controller

XILab, whose User Manual is available at [19], gives the possibility to precisely move simultaneously all the stages connected to one or more controller. Once the controller is connected to the stages, to an electrical outlet and to the computer, it starts flashing and it should be detected by the computer; Figure 3.4 illustrates the meaning of the possible flashes.

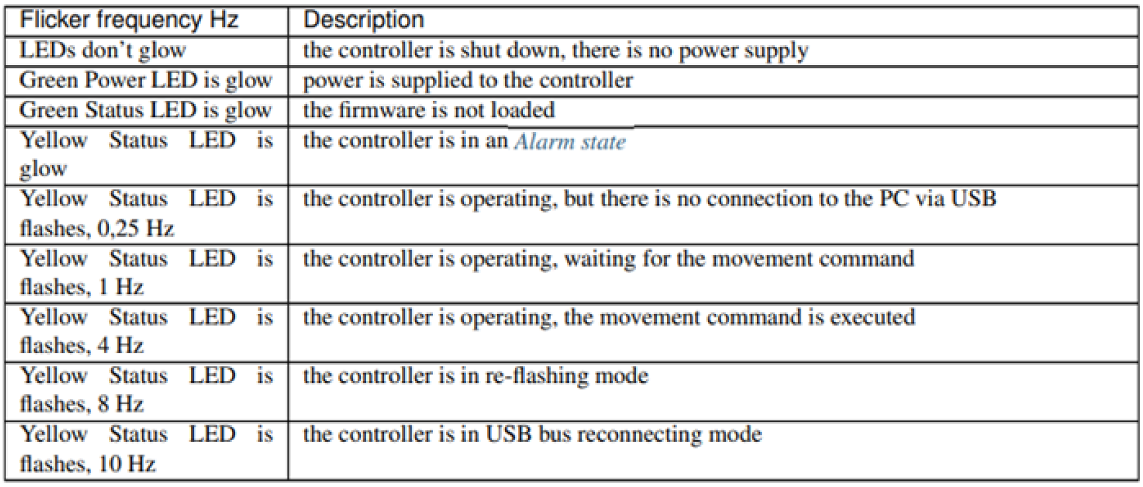

Flicker frequency Hz	Description
LEDs don't glow	the controller is shut down, there is no power supply
Green Power LED is glow	power is supplied to the controller
Green Status LED is glow	the firmware is not loaded
Yellow Status LED is glow	the controller is in an *Alarm state*
Yellow Status LED is flashes, 0,25 Hz	the controller is operating, but there is no connection to the PC via USB
Yellow Status LED is flashes, 1 Hz	the controller is operating, waiting for the movement command
Yellow Status LED is flashes, 4 Hz	the controller is operating, the movement command is executed
Yellow Status LED is flashes, 8 Hz	the controller is in re-flashing mode
Yellow Status LED is flashes, 10 Hz	the controller is in USB bus reconnecting mode

Figure 3.4: Explanation of the controller flashes

At this point, one can open XILab software and select the desired controllers, then the main window appears, it has two possible modes: single axis and multiple axes, which are visible in the images below. During the laboratory, the multi-axis mode has been chosen, in order to control the movements in all directions simultaneously. The following part explains some of the main features and functions of the software.

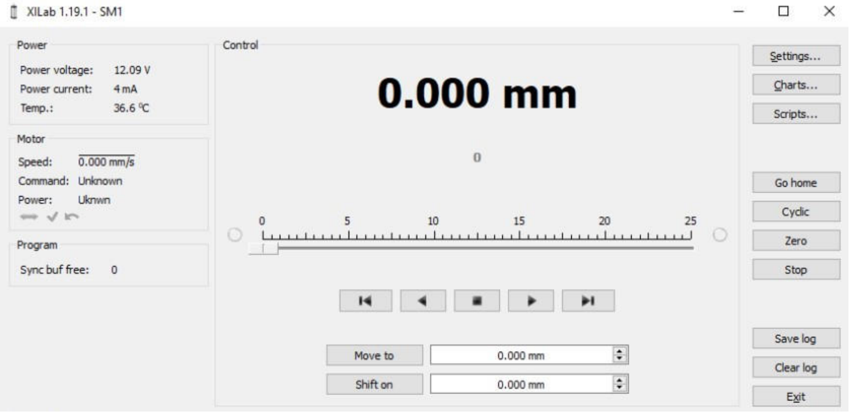
XiLab 1.19.1 - SM1

Power

Power voltage: 12.09 V
Power current: 4 mA
Temp.: 36.6 °C

Motor

Speed: 0.000 mm/s
Command: Unknown
Power: Uknwn

Program

Sync buf free: 0

Control

0.000 mm

Move to 0.000 mm
Shift on 0.000 mm

(a) XILab single-axis window

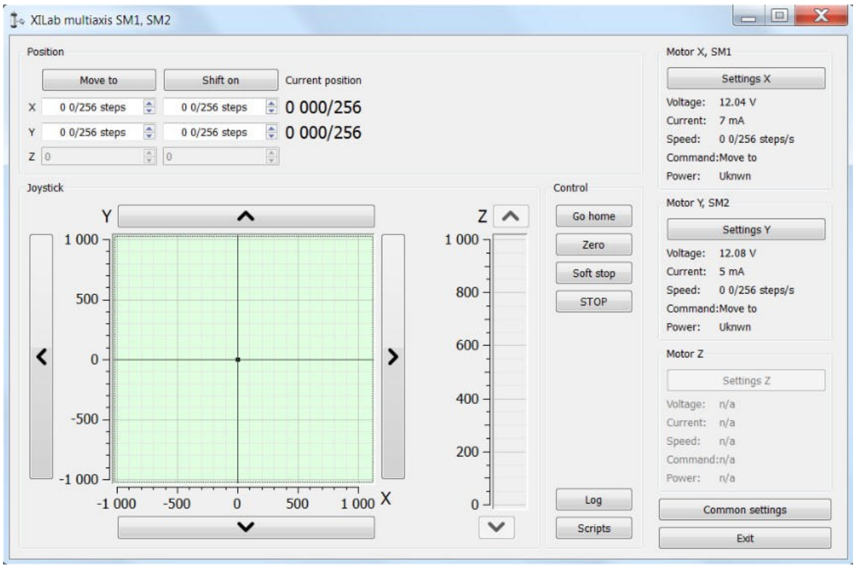
XILab multiaxis SM1, SM2

Position

Current position
X 0 0/256 steps 0 0/256 steps 0 000/256
Y 0 0/256 steps 0 0/256 steps 0 000/256
Z 0 0

Motor X, SM1

Voltage: 12.04 V
Current: 7 mA
Speed: 0 0/256 steps/s
Command: Move to
Power: Uknwn

Motor Y, SM2

Voltage: 12.08 V
Current: 5 mA
Speed: 0 0/256 steps/s
Command: Move to
Power: Uknwn

Motor Z

Voltage: n/a
Current: n/a
Speed: n/a
Command: n/a
Power: n/a

(b) XILab multi-axis window

Figure 3.5: XILab main window possible modes

3.1.1 Settings

Figure 3.7 on the side displays the window that appears by clicking on the settings button, from this it is possible to set all the required specifications, such as the working current, the maximum rotation speed, borders, limit speed, etc. The table below summarises the main specifications of 8SMC5-USB controller:

Number of axes	1 to 4 (up to 32 axes in single USB port)
Motor parameters	
Motor type	stepper/dc/servo
Current	
Stepper motor	0,1- 3 A
DC, servo	0,1- 6 A
Voltage	2-48 Vdc
Motor kinematics	
Step division (for stepper motor)	1-1/256
Maximum speed	
Stepper motor	35000 steps/s
DC, servo	800000 counts/s
Motion control	
Motion modes	move left/right, move to point, shift on delta, continuous speed, acceleration and deceleration ramps, backlash compensation mode, automatic home position calibration mode, linear interpolation, circular interpolation and etc.
Control loop	Open loop, closed loop
Compensation	
Backlash compensation	Included
Step loss compensation	Included
Positioner sensors reading	
Encoder (rotary)	Incremental quadrature encoder (TTL, RS422 up to 5MHz)
Limit switches	optron, hall sensor, microswitch
Revolution sensor	supported
Communication interface	Ethernet, USB, RS232
I/O	
Synchronization	I/O included
Joystick	Analog input (0-3V)
Output	+3V; +5V for power supplying
Motor connector	DB15F
Supplementary connector	DB25F
Position counter	40 bit
Positioner identification	One-wire interface (for Standa and other suppliers)
Protections	ESD protection, Current overload protection, Voltage overload protection, Short circuit protection, Motor hot plug/unplug protection
Operating temperature	Up to 70 degrees C

Figure 3.6: 8SMC5-USB Controller Specifications [18]

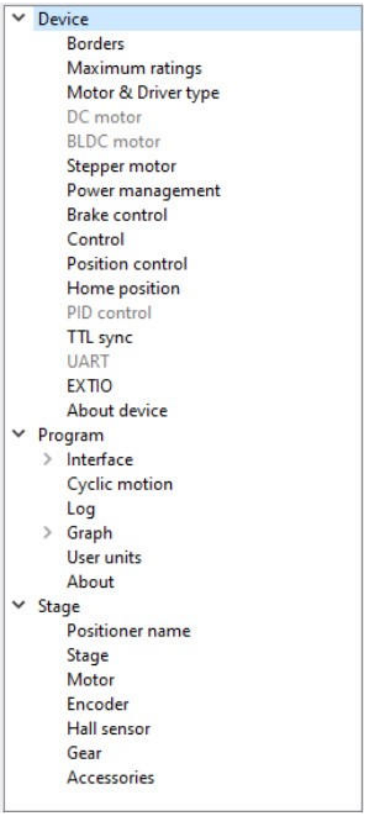

Figure 3.7: XILab Settings Main Window

Before starting to use the controller one should execute the functional test:

Try to press one of the buttons with up/down/right/left arrays, the stage should start moving, use the "soft stop" button to stop the rotation and check the power supply parameters in the Power section. If XILab main window shades red when the movement was supposed to start, it means that the controller is in the Alarm state. This may be caused by incorrect settings, wrong connection of the stage or controller malfunction.
In the next pages some of the main settings are reported with a brief explanation, divided into the three groups of Figure 3.7. Please note that it is possible to save the application settings of the first two groups ('Device' and 'Program') in an external file clicking on *Save settings to file*, then, these settings can be loaded again through the *Load setting from file* button.

- Device
  - **Borders:** it is possible to set the limit switches, i.e., values over which the motion stops, by marking *Stop at right border* and *Stop at left border*. The flag *Border misset detection* is marked if one wants to switch off the motor as soon as the limit switches are reached, because of potentially incorrectly configuration.
  - **Maximum ratings:** set the critical values such as maximum current (in [mAs]) and voltage (in [tens of mVs]) of the controller Power supply or maximum temperature (in [tenths of °C]). From here, it is also possible to mark the *Low voltage protection* flag, which turns on the option *Low voltage off* that defines the minimum voltage value of the controller power supply. Moreover, it is possible to set some desired instructions about how the software should respond when critical values are reached.
  - **Motor & Driver type:** usually is set automatically when the controller is recognised, however it allows to choose the Engine type, *DC motor, Brushless motor or Stepper motor* and the Driver type, *Discrete FET driver, Intergrate driver or External driver.*
  - **Stepper motor or DC motor:** here most of the parameters about the motor motion can be set. Some of them are illustrated:
    - *Revers* refers to the association between the motor rotation direction and the position counting direction. Change the flag if positive motor rotation decreases the value on the position counter.
    - *Move with max speed tick* makes the motor ignore the present speed and rotate at the maximum speed, specified in *Max nominal speed*.
    - *Nominal current* sets the limit current value.
    - *Current as RMS*, if this flag is checked, engine current value is interpreted as root mean square current value. Otherwise, it is interpreted as maximum amplitude value.
    - *Working speed, Acceleration and Deceleration, Steps per turn and Microstep mode* (9 modes available from a whole step to the 1/256 of a step), from here it is possible to set the relative values. Please note that in order to choose the optimal acceleration and deceleration values one should start from default values, make small shifts (start and fast stop) with gradual acceleration increase until the movement becomes unstable and disrupted sometimes. Take acceleration equal to about half of this value and deceleration about 1.5 - 2 times higher than acceleration.
    - *Backlash compensation*, if it is marked, the stage always approaches a point from one side in the number of steps specified (if positive it approaches the point from the right) and at the speed written in *Backlash compensation speed.*

    - ∗ It is also possible to choose between three feedback modes if an encoder is used.
  - **Brake control:** it gives the possibility to enable magnetic brake, setting the time between motor power on and brake off, between brake off and readiness to move, and between brake on and motor power off.
  - **Control:** here one can choose the control mode, *Control disabled, Joystick or Buttons*, and set some parameters, for instance:
    - ∗ *Low end, Center and High end*, which determine the lower border, the middle and the upper border of the joystick range respectively.
    - ∗ *Dead zone*, it is a deviation (from 0.1 to 25.5 steps) from the center position where the speed is forced to zero.
    - ∗ Moreover, in this tab one can do the joystick calibration, decide the button state (pressed or released) to be considered as the motion command, and decide some click settings.
  - **Position control:** it can be activated by the encoder and in *Threshold* field it is possible to set the number of missed steps (from 0 to 255) to be considered as an error. If the amount of missed steps exceeds the specified number of steps, the SLIP error flag is set. One can also choose the action to take between *Alarm on errors, Correct errors, Ignore errors* when an error comes.
  - **Home position:** it is a reference position. In order to calibrate it, one should press *Go home* in the main window of XiLab and observe the stage moving to the specified limit switch. At the end of it, one can press *Zero* to set the origin of the coordinate system, the described procedure is called automatic calibration.
    In the *Home position* tab it is possible to set some parameters, such as *1st move direction* (left or right), *1st move speed* (about 5-10 times lower than the working speed), *Stop after* (that should be set on limit switches), etc. One that it is worth noting is *Standoff*, which sets the distance for the final offset from the reference point (positive standoff means an offset to the right).
  - **About device:** it contains some information on the controller and allows to update the firmware if desired.

- Program
  - **Interface:** here it is possible to choose between *General Motor and Attenuator* interface and to set some preferences about it.
  - **Cyclic motion:** with this, one can configure the cyclic motion between two positions. It is activated by Cyclic button in the main window, and deactivated by Stop button in the main window. It has two possible options: *Border to border* or *Point to point.*

  - **Graph:** here some features about the charts and their interval can be decided.
  - **User units:** it allows to configure custom units, that will replace steps/counts, only in the main XILab window.

- Stage

  It contains information about stage, motor, encoder, hall sensor, ...

3.1.2 Commands

Figure 3.5b shows the multi-axis interface from which it is possible to move the stages to the desired position by selecting a point on the *Virtual joystick block*, by pressing the screen or keyboard buttons with up, down, left and right arrows, or by typing a location in the *Motion control block* under the *Move to* button. Here there is also the *Current position column*, which indicates current position in steps or calibrated units, and the *Shift on* button, that performs a shift of the specified distance from the current position. Please note that if one of the controllers is temporarily absent or disabled, the corresponding line becomes grayed out.

The current coordinates of the controllers are visualized as a dot with two lines for the X-Y plane and a line for the Z axis. The association between X, Y, Z and the relative controller is customisable, since it depends on the order in which the stages and controller are connected, and it can be modified by clicking on *Common settings* on the bottom right of the multi-axis interface.

Furthermore, from Figure 3.5b one can see the *Control block*, which has the following buttons:

- *Go home* searches for the home position independently for each of the controllers.
- *Zero* resets the current position of the motor and the value of the encoder for each controller.
- *Soft stop* executes a soft stop for each of the controllers.
- *STOP* stops every controller, resets their alarm statuses, clears their command buffers for synchronous motion and stops a script if one is running.
- *Log* opens a window with log information.
- *Scripts* opens a scripting window.

In the end, on the right there is the *Block of status indicators* for X, Y and Z axes, from which it is also possible to modify the motors' settings. At the bottom there is the *Exit* button, which performs the proper shutdown; when clicked, it sends a soft stop command to the controller, and after the stop is completed, the application sends the command of power-off.

3.2 Slit width calibration

Figure 3.8 on the side shows the provided slit, as can be seen from the picture there is a knob which controls the slit width. The nominal working value is 200 μm, with a maximum value of 2 mm. The aim of this paragraph is to find the slit width by fitting the diffraction figure for three different positions of the knob in order to obtain a graphic line which represents the relationship between the slit width and the knob position. For this reason, the diffraction theory is firstly presented, followed by the proper activity carried out at CNR-IFN laboratory and the results obtained by it.

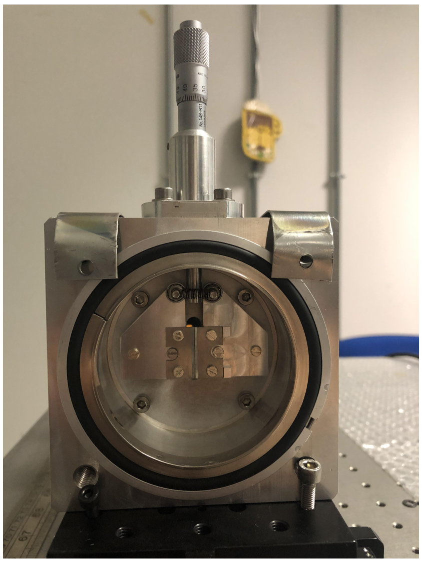

Figure 3.8: Slit picture

3.2.1 Theory of diffraction

Diffraction is a physical phenomenon which occurs every time an electromagnetic wave encounters a slit of different shapes, a screen, or another kind of obstacle. The Huygens-Fresnel principle gives a method to understand how the wavefront propagates after the obstacle, it states that every point on a wavefront can be considered as a source of spherical waves and that these secondary waves, emanated from different points, mutually interfere originating the new wavefront. The diffraction is actually visible when the obstacle size is comparable to the wavelength of the incident light, thus the diffraction figure changes with the size of the obstacle.

The pattern resulting from a single-slit diffraction is displayed in Figure 3.9, as can be seen from the image, there is a central maximum of intensity and other secondary maxima on the sides. This curve is the result of a N-sources (distant Δa from each other) interference as described by the Huygens-Fresnel principle; when these secondary waves reach a point on the screen, they are out of phase because of the different lengths they have covered, thus the intensity of the total electromagnetic field varies among the screen, creating the so-called diffraction figure.

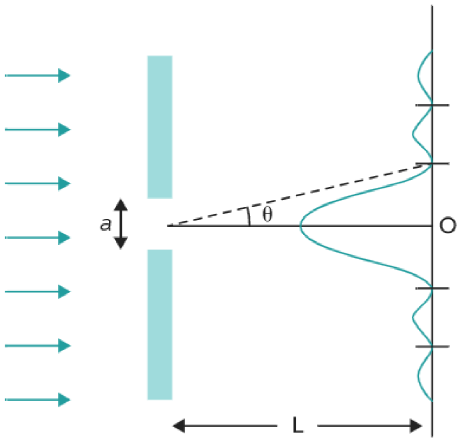

Figure 3.9: Single-slit diffraction

In order to derive the formula that describes the diffraction figure, it is necessary to use the phasors' method, which gives the expression of the electromagnetic field E_P in a point P on the screen.
In this case, $N \to \infty$ and Δa $\to 0$, thus the following formula is obtained:

$$E_P = E_{max}\frac{sin(\alpha/2)}{\alpha/2}, \tag{3.1}$$

where E_{max} is the electric field magnitude of the central maximum ($\theta = 0$) and alpha is the angle between the first and the last phasor and it is equal to $\frac{2\pi}{\lambda}asin\theta$. At this point, it is easy to find the intensity expression since it is proportional to the square of E_P; using the definition $sinc(x) = \frac{sin(\pi x)}{\pi x}$, it follows:

$$I(\theta) = I_{max}\left(\frac{sin\left(\frac{\pi asin(\theta)}{\lambda}\right)}{\frac{\pi asin(\theta)}{\lambda}}\right)^2 = I_{max}sinc^2\left(\frac{asin(\theta)}{\lambda}\right) \tag{3.2}$$

From formula (3.2) one can see that there are points of minimum, points of local maxima, and a point (when $\theta = 0$) where there is the central maximum:

- The minima occur when $sin\left(\frac{\pi asin(\theta)}{\lambda}\right) = 0$, which implies

$$sin(\theta) = m\frac{\lambda}{a} \qquad \text{for m = } \pm 1, \pm 2, ...; \tag{3.3}$$

- and the secondary maxima when

$$sin(\theta) = (2m+1)\frac{\lambda}{2a} \qquad \text{for m = } \pm 1, \pm 2, ... \tag{3.4}$$

Therefore, the shape of the diffraction figure depends on the value of a and λ.

For instance, given a fixed slit width, if the incident light is monochromatic, then there is only one diffraction figure; otherwise, for polychromatic light the diffraction figure will have a white central maximum and then every wavelength will have their own secondary maxima, located farther from the central maximum when λ is increasing, as shown in Figure 3.10a below.

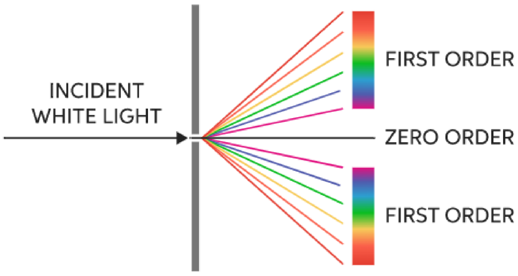

(a) Single-slit diffraction of polychromatic light

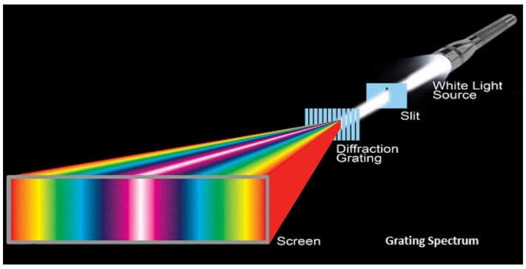

(b) Diffraction grating and spectrum of polychromatic light

This is the principle behind every spectrometer, in fact spectrometers include diffraction gratings, these are optical elements that diffract light into its spectral components (see Figure 3.10b), as described for the single-slit diffraction. The groove density, depth and profile of the diffraction grating determine the spectral range, the efficiency, the resolution and the performance of the spectrometer.

3.2.2 Image acquisition and relative fitting

In order to extract the value of the slit width for a fixed position of the knob, one can use the knowledge of the intensity trend expressed by the equation (3.2) and fit the irradiance profile obtained when the slit is illuminated. The optical bench disposition used to take the images is displayed in Figure 3.11 below.

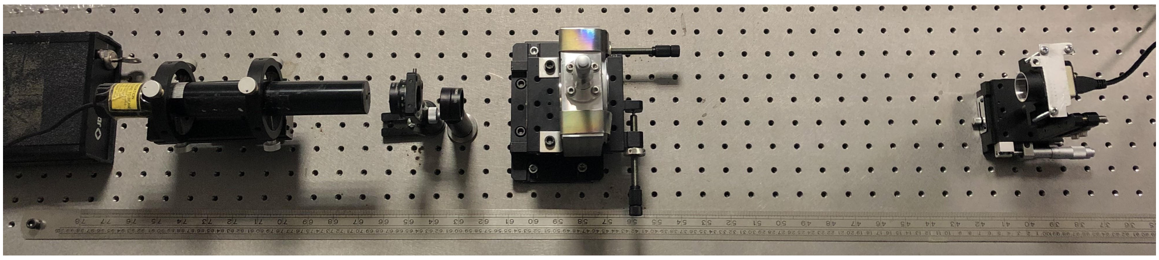

Figure 3.11: Optical bench disposition from left to right: laser, two absorptive filters, slit, CCD camera

The slit has been located on a translator to be able to align it in the best possible way; before it there are two absorptive filters, which lower the intensity so that it does not saturate, and the laser (JDSU 1100 Series red helium-neon) that illuminates the slit; then a camera on another translator has been used to take the images. The camera model is DCC1545M - USB 2.0 CMOS, it has 1280x1024 pixels with resolution of 1.3 Mpix and pixel size equal to 5.2 μm; the whole documentation is available at [20].

Every image has been taken at two different exposure times:

- One at 46.371 ms, at which the central peak saturates, while the secondary ones are well recognisable (top image in picture 3.12);
- the other one at 13.855 ms, in order to be able to clearly observe also the central maximum (bottom image in picture 3.12).

The two images have been combined together to reach an high dynamic range HDR, which is the ratio between the highest brightness value and the lowest brightness value. This allows to observe both the central maximum and the secondary maxima in the same image.

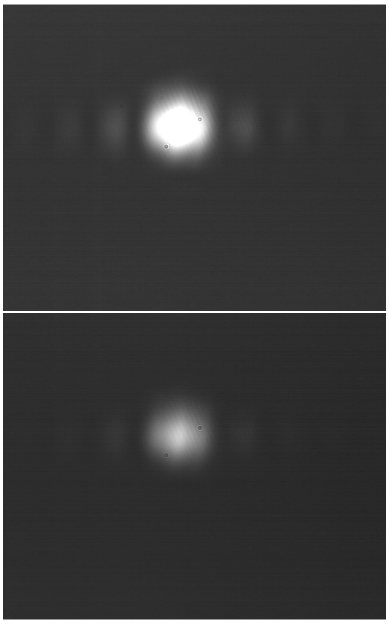

Figure 3.12: Example of images obtained by the camera when the knob is at 3 mm, with 46.371 ms (top image) and 13.855 ms (bottom image) as exposure time

The work has been done for three different positions of the knob: at 5mm, at 3 mm and at 0mm. For each position of the knob, we have taken 5 images with the laser switched on (signal) and 5 with the laser switched off (dark); using Matlab we have averaged both groups and subtracted the dark from the signal images.

Matlab gives also the possibility to realise the fitting of a given set of data choosing the curve trend expected, that in this case is $Asinc^2(.)$. Once obtained the signal-dark average images for each exposure time, the relative irradiance profiles have been extracted by selecting a line going through the diffraction figure. In order to normalise the irradiance profiles with respect to the exposure time, we have multiplied the irradiance by a factor of $\frac{46.371ms}{max\ expTime}$ for the image at the higher exposure time and $\frac{13.855ms}{max\ expTime}$ for the other image; after it, we have normalised the profiles with respect to the the maximum value of the irradiance.
At this point, we have fitted both images separately in order to combine them by keeping the one at the maximum exposure time for the secondary peaks and the other one for the central peak.
The fitting has been realised using Matlab commands *fittype* and *fit*, giving to the former the function $I_0 sinc^2(\alpha(x-x_0))$ as input, and to the *fit* function what *fittype* returns, together with the starting point vector and the ranges into which look for the parameters' optimal values. Please note that the mentioned formula results from the equation (3.2) using the approximation valid for small θ: $sin(\theta) = x/L$, where x is the position along the screen and L is the distance between the slit and the camera. The parameters that Matlab has to determine are:

- $\alpha = \frac{a}{L\lambda}$, where a is the value of the slit width, λ is the laser wavelength, equal to 632.8 nm, and L=42 cm is the distance between the slit and the camera.
- x_0, the position of the central maximum.
- I_0, the value of the central maximum.

The initial value of α has been chosen looking at the position x_{min} of the first minimum, for which it is valid $\alpha = 1/(x_{min} - x_0)$ using the equation (3.3); the initial values of the other parameters have been guessed by looking at the irradiance profile. After having executed the *fittype* and *fit* functions, we have plotted the fitting to see the comparison with the data and to optimise it by trying different ranges in which Matlab should search. Once the optimal fitting is ready, one can see the value chosen by Matlab for α and extract the slit width a as:

$$a = L\lambda\alpha \tag{3.5}$$

The described procedure has been applied to the taken images for the three positions of the knob, the following paragraph shows the fittings obtained and the relative values found for the slit width.

3.2.3 Results

- **Knob at 0 mm**

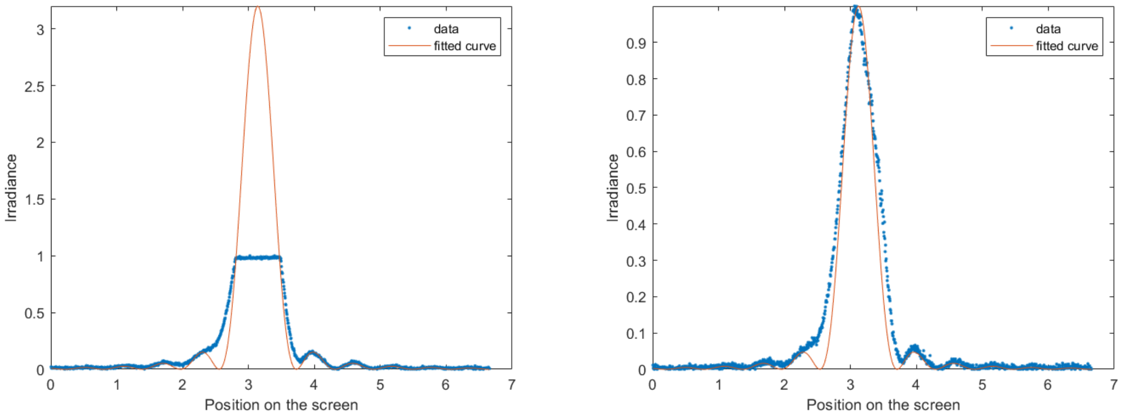

(a) Exposure time equal to 46.371 ms

(b) Exposure time equal to 13.855 ms

Figure 3.13: Diffraction figure with relative fitting, for knob at 0mm

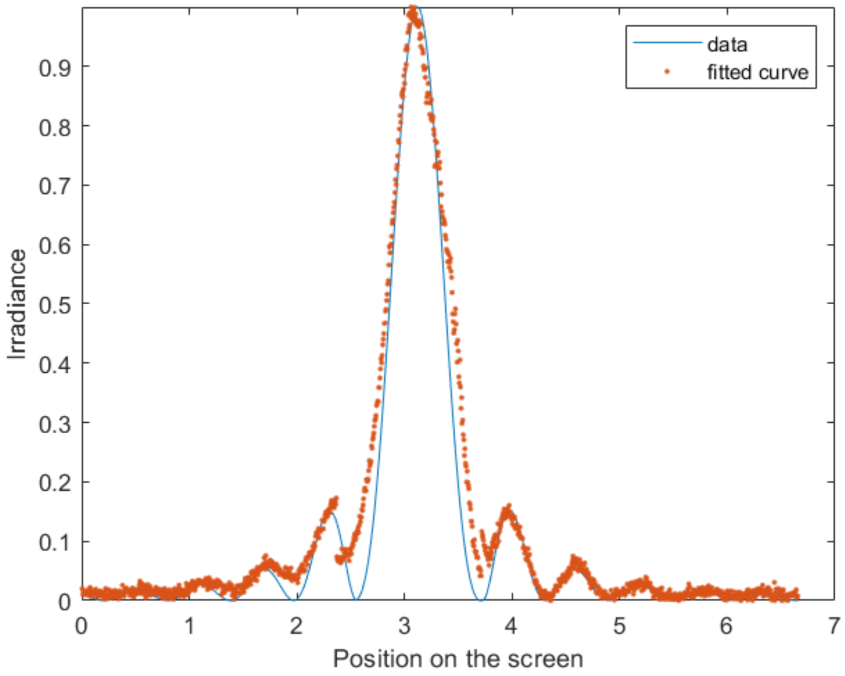

Figure 3.14: HDR diffraction figure with relative fitting for knob at 3mm

Figure 3.14, as described earlier, is the combination of Figures 3.13a and 3.13b.
The Matlab function *fit* returned 1.708 mm^{-1} as the optimal value for α. Thus, it follows: $a = 0.4539$ mm, using equation (3.5).

- **Knob at 3 mm**

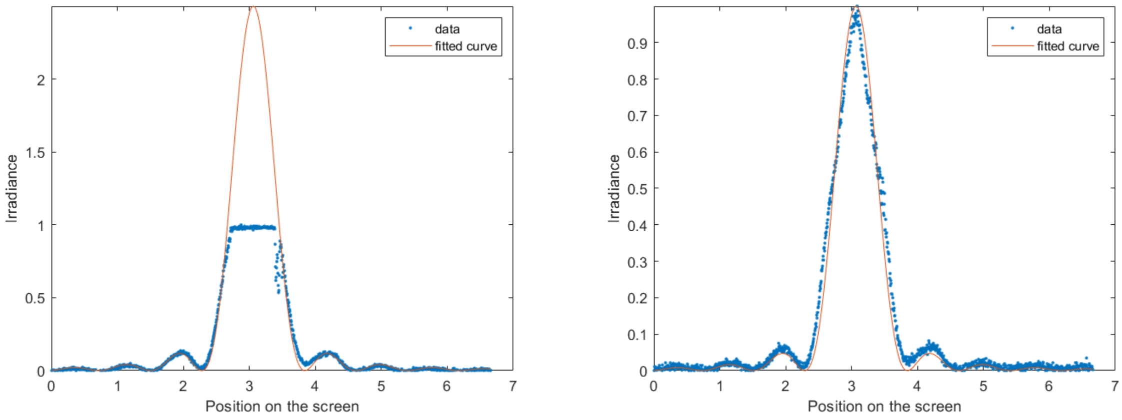

(a) Exposure time equal to 46.371 ms (b) Exposure time equal to 13.855 ms

Figure 3.15: Diffraction figure with relative fitting, for knob at 3mm

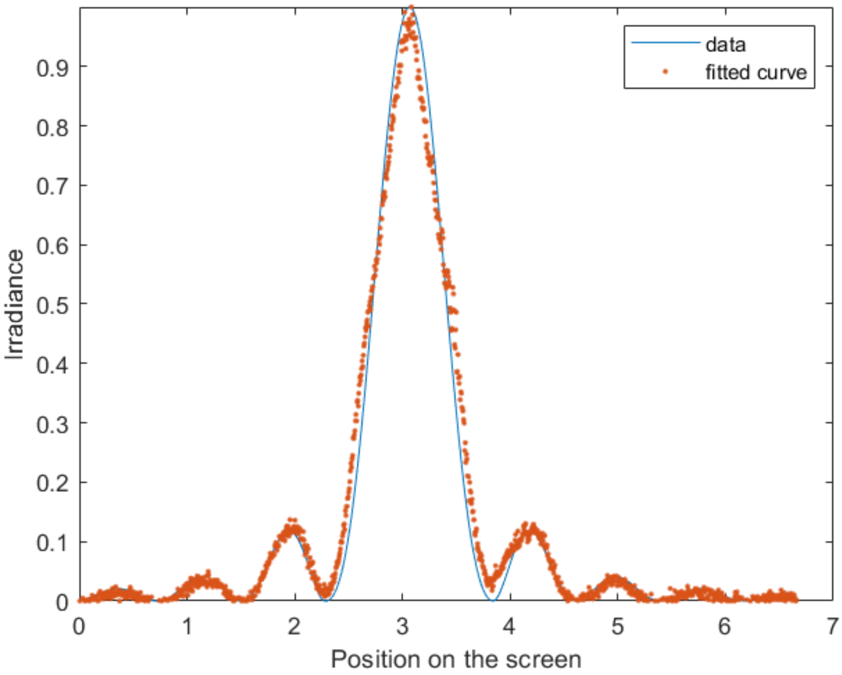

Figure 3.16: HDR diffraction figure with relative fitting for knob at 3mm

Figure 3.16, as described earlier, is the combination of Figures 3.15a and 3.15b. The Matlab function *fit* returned 1.283 mm^{-1} as the optimal value for α. Thus, it follows: $a = 0.3410$ mm, using equation (3.5).

- **Knob at 5 mm**

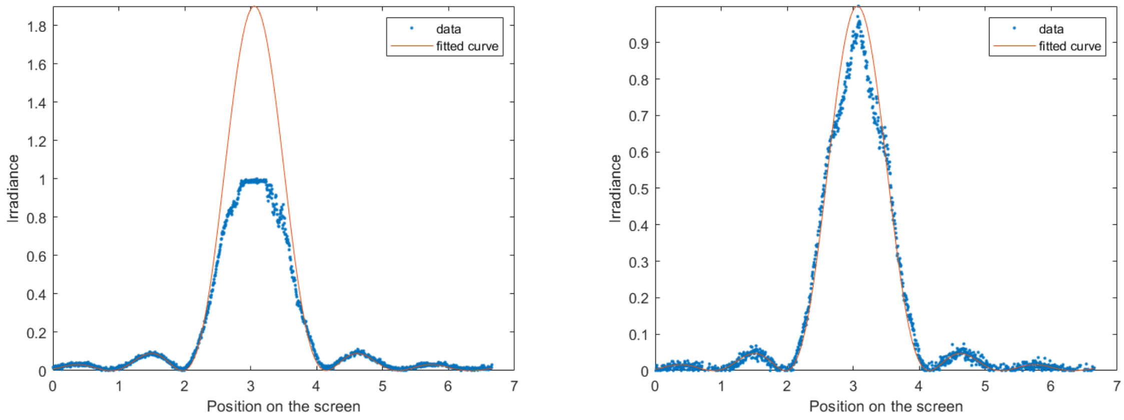

(a) Exposure time equal to 46.371 ms (b) Exposure time equal to 13.855 ms

Figure 3.17: Diffraction figure with relative fitting, for knob at 5mm

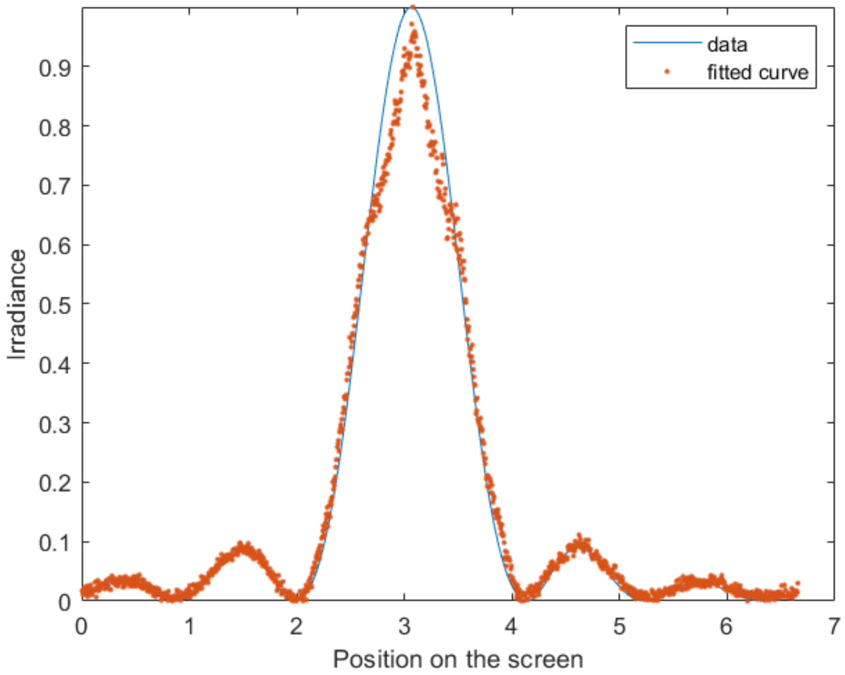

Figure 3.18: HDR diffraction figure with relative fitting for knob at 5mm

Figure 3.18, as described earlier, is the combination of Figures 3.17a and 3.17b.
The Matlab function *fit* returned 0.918 mm^{-1} as the optimal value for α. Thus, it follows: $a = 0.244$ mm, using equation (3.5).

It is worth noting that in order to be able to obtain a proper fitting for the exposure time equal to 46.371 ms (when the central maximum saturates), it has been necessary to set $I_0 \neq 1$, such that the fitting suits the secondary maxima and overcomes the saturation of the central one. Moreover, one can observe that some minima near the central maximum are not exactly at zero, this is probably due to its high brightness. From the figures it can be seen also that the central maximum becomes larger as the slit width gets smaller, accordingly to the theory of diffraction.
To conclude, Figure 3.19 displays the relationship between the slit width and the position of the knob:

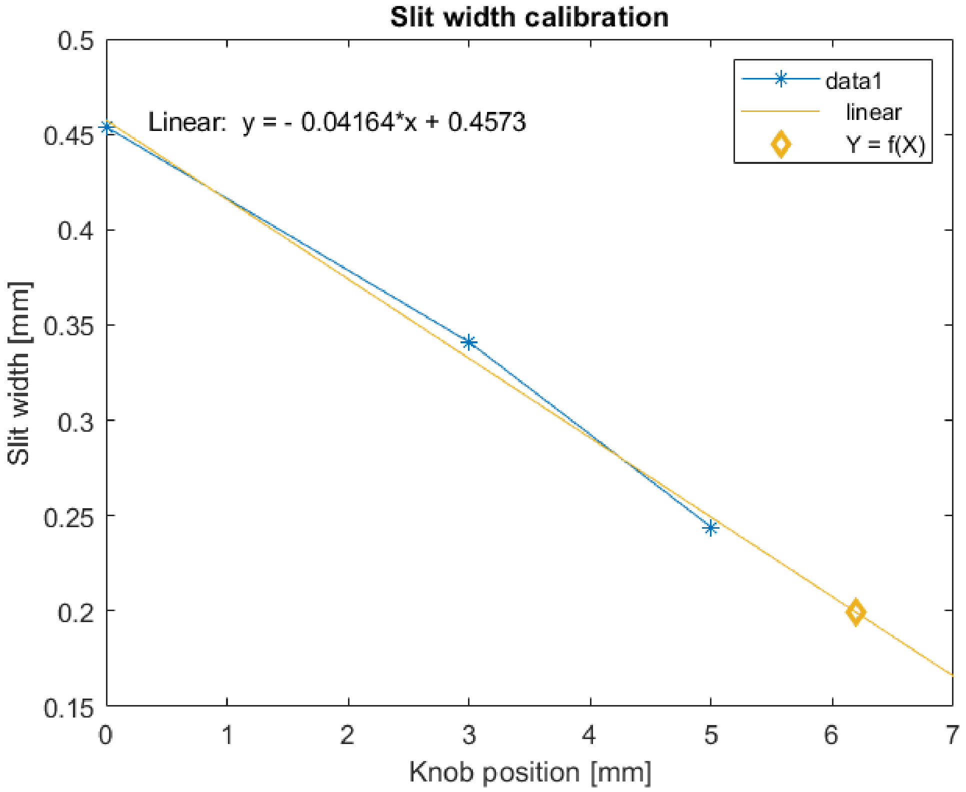

Figure 3.19: Slit width calibration

From the graphic above, one can see that the couples (knob position-slit width) are located approximately on a line, the fitting line has been added in order to see which width corresponds to every position of the knob. Furthermore, the point for which the width is equal to 0.2 mm has been marked with a diamond, because this should be the working value; in this point the knob position is 6.19 mm. It is worth noting that for an accurate calibration one should extract the value of the slit width for more positions of the knob, thus this calibration will be completed in the near future.

Conclusions

FUV/EUV imaging spectrometry is essential in many fields regarding the Solar System, such as the study of the auroral footprints and polar magnetosphere of gas or ice giant planets, as well as the characteristics of the upper atmosphere or exosphere of their satellites, or in the characterisation of the geological nature and composition of the planetary surface, or in ice-detection, exc. Therefore, future space missions will need an UV spectrometer in their payload.
The Italian team composed of CNR-IFN, INFN, Politecnico di Milano, aims to provide a cutting-edge spectrometer by overcoming most of the limits of the previous ones: it will have a simplified scheme, an optimised aberration compensation thanks to two spherical variable-line-spaced gratings, two channels with optimized components for each one, and a solar blind detector with photon counting capability on chip, characterized by high spatial resolution, shorter observations integration time, high dynamic range, improved detection limit, and longer lifetime. These novel detectors could also find other new applications, such as counting particles in in-situ measurements.

Currently, an EUV channel demonstrator is under realisation at CNR-IFN laboratory in order to test the performances of the system; the optical design and the opto-mechanical design of the vacuum chamber have been completed, the plane grating prototypes have been fabricated, as well as a novel photon counting MCP detector. Then, the system will be integrated in clean-room and test in vacuum.

In the next months the detector prototype will be assembled and characterized in vacuum, then it will be mounted on the demonstrator model of the EUV channel; meanwhile, the alignment of the components is going to be realised on a vacuum-compatible breadboard. Then, in order to test the spatial resolution of the detector, an hollow cathode lamp, that consists of a glass tube containing a cathode, an anode, and a buffer noble gas, will be used. The noble gas that has been chosen is the Argon, since it has two doublets; the one we are interested in is at 92.0 & 93.2 nm, hence the aim of the test is to verify that these peaks are discernible. Moreover, the detector response will be tested in different conditions, for example varying the source intensity, the voltage, the slit width, verifying for each situation the resolution, the dynamic range, the SNR, or other features.

Bibliography

[1] S Alan Stern. ≪The lunar atmosphere: History, status, current problems, and context≫. In: *Reviews of Geophysics* 37.4 (1999), pp. 453–491.

[2] C. A. Dukes and M. J. Schaible. *The Lunar Surface-Exosphere Connection*. 2017. URL: `https://www.azom.com/article.aspx?ArticleID=14015`.

[3] M. G. Pelizzo et al. *Spectroscopic observations of Moon in the ultraviolet*.

[4] Eric Quémerais et al. ≪PHEBUS on Bepi-Colombo: post-launch update and instrument performance≫. In: *Space Science Reviews* 216.4 (2020), pp. 1–23.

[5] Jean-François Mariscal et al. ≪Probing of Hermean Exosphere by Ultraviolet Spectroscopy: instrument presentation, calibration philosophy and first lights results≫. In: *International Conference on Space Optics—ICSO 2010*. Vol. 10565. SPIE. 2017, pp. 252–258.

[6] M. G. Pelizzo et al. *PLanet extreme Ultraviolet Spectrometer project*. Jan. 12, 2022.

[7] *ALICE*. ESA. URL: `https://www.esa.int/Science_Exploration/Space_Science/Rosetta/ALICE`.

[8] *LRO Spacecraft Instruments*. NASA. URL: `https://www.nasa.gov/mission_pages/LRO/spacecraft/index.html`.

[9] *Instrument Information*. NASA. URL: `https://pds.nasa.gov/ds-view/pds/viewInstrumentProf` `jsp?INSTRUMENT_ID=UVS&INSTRUMENT_HOST_ID=JNO`.

[10] Jean-Loup Bertaux et al. ≪SPICAV on Venus Express: Three spectrometers to study the global structure and composition of the Venus atmosphere≫. In: *Planetary and Space Science* 55.12 (2007), pp. 1673–1700.

[11] P Zuppella et al. ≪Optical subsystems calibration and derived radiometric instrument response of the PHEBUS spectrometer on board of the BepiColombo Mission≫. In: *Journal of Instrumentation* 7.10 (2012), P10023.

[12] *Bepi-Colombo*. ASI. URL: `https://www.asi.it/en/planets-stars-universe/solar-system-and-beyond/bepi-colombo/`.

[13] Jan van Casteren and M Novara. ≪BepiColombo mission≫. In: *Memorie della Societa Astronomica Italiana* 82 (2011), p. 394.

[14] *PLanet Ultraviolet Spectrometer - PLUS*. June 17, 2019. URL: ?.

[15] MG Pelizzo et al. «The PLanetary extreme Ultraviolet Spectrometer Project». In: *Astronomical Optics: Design, Manufacture, and Test of Space and Ground Systems III*. Vol. 11820. SPIE. 2021, pp. 348–355.

[16] Michela Uslenghi et al. «Development of a novel photon counting detector for UV spectrographs». In: *X-Ray, Optical, and Infrared Detectors for Astronomy X*. Vol. 12191. SPIE. 2022, pp. 841–850.

[17] E Fabbrica et al. «Design of MIRA, a low-noise pixelated ASIC for the readout of microchannel plates». In: *Journal of Instrumentation* 17.01 (2022), p. C01047.

[18] *8SMC5-USB - Stepper & DC Motor Controller*. URL: `https://www.standa.lt/products/catalog/motorised_positioners?item=525`.

[19] *8SMC5-USB User Manual*. URL: `https://doc.xisupport.com/en/8smc5-usb/8SMC5-USB.pdf`.

[20] *DCC1545M - USB 2.0 CMOS Camera*. URL: `https://www.thorlabs.com/catalogpages/obsolete/2020/DCC1545M.pdf`.